

## Examining the Magnetic Field Strength and the Horizontal and Vertical Motions in an Emerging Active Region

Chia-Hsien Lin<sup>1</sup> · Yu-Che Chen<sup>2</sup>

© Springer ●●●

**Abstract** Earlier observational studies have used the time evolution of emerging magnetic flux regions at the photosphere to infer their subsurface structures, assuming that the flux structure does not change significantly over the near-surface layer. In this study, we test the validity of this assumption by comparing the horizontal and vertical motions of an emerging active region. The two motions would be correlated if the emerging structure is rigid. The selected active region (AR) NOAA 11645 is not embedded in detectable preexisting magnetic field. The observed horizontal motion is quantified by the separation of the two AR polarities and the extension of the region. The vertical motion is derived from the magnetic buoyancy theory. Our results show that the separation of the polarities is fastest at the beginning with a velocity of  $\approx 4 \text{ Mm hr}^{-1}$  and decreases to  $\leq 1 \text{ Mm hr}^{-1}$  after the main growing phase of flux emergence. The derived thick flux-tube buoyant velocity is between 1 and 3  $\text{Mm hr}^{-1}$  while the thin flux-tube approximation results in an unreasonably high buoyant velocity, consistent with the expectation that the approximation is inappropriate at the surface layer. The observed horizontal motion is not found to directly correlate with either the magnetic field strength or the derived buoyant velocities. However, the percentage of the horizontally oriented fields and the temporal derivatives of the field strength and the buoyant velocity show some positive correlations with the separation velocity. The results of this study imply that the assumption that the emerging active region is the cross section of a rising flux tube whose structure can be considered rigid as it rises through the near-surface layer should be taken with caution.

---

✉ C.-H. Lin  
chlin@jupiter.ss.ncu.edu.tw  
Y.-C. Chen  
commanderchen@gmail.com

<sup>1</sup> Graduate Institute of Space Science, National Central University, Chung-Li, Taoyuan, Taiwan

<sup>2</sup> Department of Atmospheric Science, National Central University, Chung-Li, Taoyuan, Taiwan

---

**Keywords:** Active Regions, Magnetic Fields; Active Regions, Models; Active Regions, Structure; Active Regions, Velocity Field

## 1. Introduction

Sunspots and solar active regions are zones with very concentrated magnetic fields on the solar surface. How these regions are formed is one of the fundamental problems in the study of solar magnetism. The formation process can be divided into two problems: the first one is how the magnetic fields are transported to the surface, and the second one is how the sunspots and active regions are formed from these fields after they rise to the surface.

The first problem has been studied for more than half a century. Parker (1955) was the first to propose magnetic buoyancy as a viable mechanism to bring a strand of toroidal field to the surface. Since then, many works have been conducted to include more realistic effects to the model of magnetic flux transport through the solar convective zone. For instance, Schüssler (1979) considered the effects of differential rotation, flux loss and convective motions, and also derived a mathematical expression for flux tubes with arbitrary sizes. They found from their numerical simulation that the shape of the flux tube changes during the rising. Caligari, Moreno-Insertis, and Schüssler (1995) included the effects of spherical geometry and differential rotation in their numerical simulations, and reported that their results were consistent with observed asymmetries, AR tilt angles and emergence latitudes. Fan (2008) examined the effects of magnetic twist and Coriolis force. Weber, Fan, and Miesch (2011) applied a thin flux-tube model in a rotating spherical shell of turbulent convective flows. The validation of these models has usually been based on whether a model can qualitatively produce the observed general properties such as Hale's law, hemispheric tilt and active latitudes. The detailed flux transport processes implemented in these models, however, is much harder to verify because the process takes place in the invisible solar interior. The magnetic fluxes only become observable after they emerge from the photosphere. Some earlier studies used the temporal evolution of emerging flux regions (EFRs) or emerging active regions (EARs) as a means to probe the invisible part of the flux-tube structure and dynamics. Specifically, they considered the time sequence of the observed EFRs and EARs as snapshots of different layers of the rising magnetic structure from top down, and developed methods to reconstruct the subsurface structures (Tanaka, 1991; Leka *et al.*, 1996; Chintzoglou and Zhang, 2013). These studies were based on the assumption that the structure does not change significantly as it crosses the surface, which, however, has not been verified observationally, and contradicts some recent simulation results (*e.g.*, Rempel and Cheung, 2014).

The second problem is how active regions are formed from the fields being brought to the surface. Are they the result of a rising field structure intersecting the surface, or are they formed by turbulence and/or convergence of previously emerged small fields (*e.g.*, Lites, Skumanich, and Martinez Pillet, 1998)? Although in this case the process is observable, it is difficult to decipher the actual physical mechanisms. This is because the gas density and pressure

change radically over a very thin layer across the surface, specifically, the plasma  $\beta \equiv P_{\text{gas}}/P_{\text{mag}}$  changes from  $\beta \gg 1$  in the convection zone to  $\beta \approx 1$ , which means that the plasma and magnetic field interact dramatically in this layer. As a result, the fields are distorted, deformed, and restrengthened by the plasma motions at this near-surface layer. In addition, since the physical scales of many complex processes, such as turbulence, flows, convection, and others, become comparable with the scale of the magnetic flux tube, simplifications such as the thin flux-tube approximation and the anelastic assumption are no longer valid in this layer. Recent simulations have shown that the structure of the flux tube can be significantly changed during flux emergence across the near-surface layer (*e.g.*, Rempel, 2011; Rempel and Cheung, 2014). Brandenburg *et al.* (2011) numerically demonstrated that a negative effective magnetic pressure instability (NEMPI) can lead to the formation of bipolar regions. A comprehensive review can be found in Cheung and Isobe (2014). These models, simulations, and assumptions should be verified before being applied to infer the physics associated with EFRs and EARs.

An early study to test the magnetic buoyancy theory was conducted by Chou and Wang (1987). They derived the buoyant velocities of 24 emerging bipoles based on the magnetic buoyant force of the thick flux-tube approximation (Schüssler, 1979), and compared them with observationally determined separation velocities of the bipoles. They found no correlations between the two velocities. However, their study utilized line-of-sight (LOS) magnetograms, and was based on the simplification that the separation speed and buoyant speed of a bipole can be considered constant during the emergence. More recently, improved observational and analysis techniques have enabled more accurate examination of the magnetic and velocity fields of EFRs and EARs. Lites, Skumanich, and Martinez Pillet (1998) conducted a high spatial resolution examination of the vector magnetic field and Doppler velocity field patterns of three young bipolar active regions in which flux emergence could still be detected. They found that the emerging horizontal magnetic elements had field strength from  $\approx 200$  to 600 G and upward rising speeds  $\approx 1 \text{ km s}^{-1}$ . These horizontal field elements rapidly moved away from the site of emergence to become more vertically oriented, after which their field strength increased to kilogauss values. Based on their results, they suggested that the EFRs were caused by the emergence of subsurface structures rather than by organized flows near the surface. Kubo, Shimizu, and Lites (2003) examined the internal structure of an emerging flux region. They divided the EFR into three regions: the main bipolar region, two small emerging bipoles near the well-developed leading sunspot of the main bipole, and the remaining part of the main bipolar region. By comparing the evolution of the field strengths and filling factors of the main bipole and the small emerging bipoles, they deduced that the reorganization of the magnetic fields by convective collapse (Parker, 1978) and flux concentration is a possible mechanism for the evolution of the EFRs. The subject of these two studies was flux emergence in preexisting active regions. Centeno (2012) studied the emergence of two active regions that were isolated and not embedded in preexisting fields. They analyzed the relationship between the Doppler velocities and the inclination angle, relative to LOS, of the magnetic field vectors of all

magnetic flux elements in the emerging active regions. They found that the fields connecting two polarities were horizontally oriented with strong upward plasma velocities while the magnetic fields in the footpoints were vertically oriented with downward plasma velocities. In these studies, every magnetic flux element was treated as independent, and their statistical analysis was the basis to deduce the possible formation mechanism(s) of their selected regions.

The aim of the present article is to test the assumption that an emerging active region is formed by the emergence of a subsurface flux structure whose dynamics is mainly governed by the magnetic buoyancy mechanism and whose structure can be considered rigid as it moves across the near-surface layer. For an ideal rigid structure, its vertical and horizontal motions, being the two perpendicular components of the total motion, are expected to be correlated. Our strategy is to choose an EAR that qualitatively resembles the emergence of a single flux tube, and check whether any dependence exists between its horizontal and vertical motions. The vertical motion is represented by the buoyant velocity as derived by Chou and Wang (1987). We calculate the buoyant velocities in both thin flux-tube and thick flux-tube approximations to check whether the approximations are valid in the EAR. The horizontal motion is measured by the changing rates of the separation of the two polarities, the “extension” of the region, and the area of the entire region. We define “extension” as the size of the region in the direction perpendicular to the line connecting the two polarities.

## 2. Data

The vector magnetograms used in this work are derived from the data taken by the *Helioseismic and Magnetic Imager* instruments (HMI: Schou *et al.*, 2012) on board the *Solar Dynamics Observatory* (SDO: Pesnell, Thompson, and Chamberlin, 2012). The computation of the HMI vector field products has been explained in detail by Hoeksema *et al.* (2014), and a brief description is given here for completeness. The data are full-disk Stokes polarization parameters of the spectral line Fe I 6173 Å sampled at six equally spaced wavelengths. The Stokes vectors are then processed by the Very Fast Inversion of the Stokes Vector (VFISV) code, which is implemented using the Milne-Eddington approximation model of the solar atmosphere. Although the original observation cadence is 45 s, the data are averaged over a 16-minute tapered window during the VFISV computation, rendering a cadence of 12 min. The results will be referred to as “ME” hereinafter. The ME vector magnetograms are full-disk images of the total field,  $|B|$ , inclination angle,  $\theta_B$ , and azimuth angle,  $\phi$ . The inclination angle is measured relative to the line-of-sight (LOS) direction, with  $0^\circ$  pointing out of the image and  $180^\circ$  into the image. The azimuth angle is measured counterclockwise (CCW) from the solar North, and contains the  $180^\circ$  ambiguity. In addition, due to a combination of satellite and instrument roll angles, the ME data are rotated by approximately  $180^\circ$  CCW relative to the actual solar images (Sun, 2013). Since the analysis of this study is indifferent to such rotation, the ME data were not corrected for the rotation, except for visualization purpose.

In addition to the full-disk magnetograms, HMI pipelines also provide active region patches (HARPs), which are patches of emerging active regions automatically detected and tracked. The detection and tracking are based on photospheric LOS magnetograms and intensity images. The  $180^\circ$  azimuth ambiguity is resolved using Metcalf’s minimum energy method (Metcalf, 1994; Hoeksema *et al.*, 2014). The geometric information from HARPs is subsequently used to calculate various space-weather related quantities at each time step to create Spaceweather HMI Active Region Patches (SHARPs) <sup>1</sup>. Two types of vector magnetic field data are offered by SHARP: data in the CCD coordinates (`hmi.sharp_720s`) and data that are remapped using a Lambert Cylindrical Equal-Area projection procedure (`hmi.sharp_cea_720s`) such that the field quantities appear as if they were observed directly overhead (Calabretta and Greisen, 2002; Sun, 2013). The former data product, which will be referred to as “SHARP”, contains total field, inclination angle and disambiguated azimuth angle. The inclination angle is relative to the LOS, and the azimuth angle is measured CCW from the solar North. The mapped data series, which will be called “CEA” in this paper, contains three field vectors,  $B_r$ ,  $B_\theta$  and  $B_\phi$ , where  $\hat{r}$ ,  $\hat{\theta}$ , and  $\hat{\phi}$  are the basis vectors of a heliocentric spherical coordinate system (Sun, 2013).

### 3. Observations

The subject of this study is the emergence of AR 11645. Figure 1 illustrates the location of its emergence on the solar disk as observed by HMI line-of-sight magnetogram. The area of the flux-emergence region and the sign of the magnetic flux concentration can be seen in more detail in Figure 2. The two white crosses mark the approximate centers of the two main polarities when the average total-field strength of the whole emerging active region reaches maximum. The figure shows that the area was initially free of preexisting magnetic field and surrounded by a ring of predominantly negative field. A small positive flux began to appear between the two white crosses at approximately 12:58 UT on 2 January 2013. As this positive region gradually increased its field strength, multiple regions with mixed polarities rapidly appeared between the two white crosses to fill the region. Although many of these new fluxes did not show a preferred polarity orientation when they first emerged, they gradually oriented themselves along the East-West direction, with the positive pole moving toward the right (solar West) and the negative pole to the left, leading the whole region to a bipolar configuration. This is consistent with Hale’s law. The spatial range of the emergence analyzed in this study is within  $\pm 20^\circ$  in longitude, from the perspective of the SDO instruments.

Because of the detection methodology, the HARP automated procedure begins to record the data of an emerging flux region only after the LOS magnetic field of the region has become sufficiently strong and a sunspot is seen in the intensity image. Therefore, while the SHARP and CEA magnetograms can provide the radial and horizontal components of the field without ambiguity, they

---

<sup>1</sup><http://jsoc.stanford.edu/doc/data/hmi/sharp/sharp.htm>

often do not include the earliest stage of flux emergence when the field is mostly horizontal and no sunspot has formed. Since the selected emerging active region is located close to the disk center, we expect the difference between the LOS and radial directions to be small. Therefore, in this study, we mainly used ME data, and incorporated CEA data to check for the errors caused by the projection effect.

## 4. Analysis

### 4.1. Coalignment of ME and CEA images

The ME data are recorded in CCD coordinates with a spatial size of 0.5 arcsec *per* pixel while the CEA data are mapped to a cylindrical equal-area coordinate system with a spatial size of 0.03 degree *per* pixel. The standard CEA coordinates  $(x, y)$  are related to the heliographic longitude and latitude  $(\phi, \lambda)$  as follows (Calabretta and Greisen, 2002; Sun, 2013):

$$\begin{aligned} x &= \phi \\ y &= (180^\circ/\pi) \sin \lambda, \end{aligned} \quad (1)$$

in which the reference point is the disk center.

To correct for the foreshortening effect in the CEA patches, a spherical coordinate rotation is applied to Equation (1) to rotate the reference point to the patch center, such that the result is an image observed directly from above (Sun, 2013):

$$\begin{aligned} x &= \arg[\sin \lambda \sin \lambda_c + \cos \lambda \cos \lambda_c \cos(\phi - \phi_c), \cos \lambda \sin(\phi - \phi_c)] \\ y &= \sin \lambda \cos \lambda_c - \cos \lambda \sin \lambda_c \cos(\phi - \phi_c), \end{aligned} \quad (2)$$

where the function  $\arg[a, b]$  means  $|\tan x| = |b/a|$ , where  $x$  is in the same quadrant with the point  $(a, b)$ .  $(x, y)$  in Equation (2) is the CEA coordinate of a point relative to the patch center, and is in radians.  $(\phi, \lambda)$  and  $(\phi_c, \lambda_c)$  are the heliographic longitude and latitude of this point and the patch center, respectively.

To ensure that the same region is cut from the ME and CEA data, the pixel coordinates of the boundary (*i.e.*, lower-left and upper-right corners) of each ME image are first transformed into  $(\phi, \lambda)$ , then transformed into the CEA coordinates using Equation (2), and finally converted into the pixel locations:

$$\text{pix} = (x, y) \frac{180^\circ}{\pi} \frac{1}{0.03} + \text{cprx}, \quad (3)$$

where **pix** and **cprx** are the pixel locations of  $(x, y)$  and the CEA patch center relative to the lower-left corner of the patch.

Figure 3 shows the comparison of some selected ME (left), and corresponding SHARP (middle) and CEA (right) images. The ME images here have been corrected for the  $180^\circ$  rotation for easier comparison with the SHARP and CEA images. It can be seen from the figure that the regions cut in the ME, SHARP, and CEA images are consistent.

## 4.2. Horizontal Motion

The geometry of the emerging flux region was measured considering the separation of the two polarities and the extension of the region in the direction perpendicular to the separation of the two polarities. The extension is used as a proxy for the width of the flux tube (see the sketch in Figure 4). For this selected EAR, the separation of the two polarities is mostly in the East-West (X) direction parallel to the Equator, and the extension of the region is mainly in the South-North (Y) direction. Therefore, for the rest of the paper, the separation and extension will be represented by  $dX$  and  $dY$ , respectively.

The temporal change of  $dX$  was determined from an X-t plot created by averaging the total field  $|B|(X, Y, t)$  over the Y direction. Since our interest is the main part of the EAR, which we loosely define as the region showing rapid flux emergence and/or with strong magnetic field, the peripheral area was not included in the averaging to avoid contamination:

$$|B|(X, t) = \frac{1}{N_{Y_2} - N_{Y_1} + 1} \sum_{j=N_{Y_1}}^{N_{Y_2}} |B|(X, Y_j, t), \quad (4)$$

where  $N_{Y_1}$  ( $N_{Y_2}$ ) is the pixel location of the lower (upper) limit of the averaging range in Y, and  $N_{Y_2} - N_{Y_1} + 1$  is the total number of pixels over which  $|B|$  is averaged. Similarly,  $dY$  as a function of time was determined from an Y-t plot created by averaging  $|B|(X, Y, t)$  over the X direction of the main part of the EAR:

$$|B|(Y, t) = \frac{1}{N_{X_2} - N_{X_1} + 1} \sum_{i=N_{X_1}}^{N_{X_2}} |B|(X_i, Y, t), \quad (5)$$

where  $N_{X_1}$  ( $N_{X_2}$ ) is the pixel address of the left (right) end of the averaging range in X, and  $N_{X_2} - N_{X_1} + 1$  is the total number of pixels over which  $|B|$  is averaged.  $dX(t)$  and  $dY(t)$  were then determined by manually tracing the edges of the area with high intensity of  $|B|$  in the X-t and Y-t images, respectively. The tracing was repeated at least five times. The level of the scattering of the five tracing results is used as a visual measure of the uncertainties in the  $dX(t)$  and  $dY(t)$ , and their subsequently derived quantities.

X-t and Y-t plots together with one tracing are shown in Figure 5 for the ME data and in Figure 6 for the CEA data. In both figures, the upper left panel is the total  $|B|$  averaged over time ( $|B|_{\text{ave}} = \int |B|(X, Y, t) dt / T$ , where  $T$  is the temporal length of the observation), which illustrates the overall shape of the EAR. The two red vertical lines in this panel mark the range in Y over which the average is done to create the X-t plot, which is placed in the lower left, and the two yellow horizontal lines mark the range in X over which the average is done to create the Y-t plot, shown in the upper right corner. The crosses in the X-t and Y-t plots mark the results of one manual edge tracing.

Note that the HMI instrument rotation was not corrected in Figure 5. Therefore, the  $|B|_{\text{ave}}$  image is rotated approximately  $180^\circ$  with respect to the real

image, and, consequently, the left and right of the X-t and Y-t plots are switched so that the left should be right and *vice versa*. The white solid lines in the X-t and Y-t plots of Figure 5 mark the starting point of the CEA data. The two horizontal stripes in the X-t and Y-t plots (at  $t \approx 130$  and  $\geq 200$ ) were caused by an unknown sudden change of the image intensity scale during the observation. To check whether the determined edges encompass the main part of the emerging flux region, several selected ME and CEA images, marked by the white crosses in the X-t and Y-t plots, were plotted in Figure 7 for ME data and in Figure 8 for CEA data. The overplotted white boxes are the manually determined boundaries. The ME images are, as noted earlier,  $180^\circ$  rotated.

The images in the first two rows of Figure 7 show that the magnetic flux change is very dynamic during the earliest stage of the emergence: small fluxes can randomly appear at random locations with arbitrary orientation, and then quickly disappear, dissipate, move away, change orientation or converge. This dynamic appearance has little resemblance with the simplistic picture of a single emerging flux rope, as sketched in Figure 4, and causes uncertainties in the determination of the boundary of the flux emergence region. Despite such difficulty, the white boxes do cover the main part of the emerging region, but do not always include all of the fluxes. We found that the excluded magnetic regions are often preexisting flux regions or flux regions that have moved away and/or dissipated quickly. Since our focus is the main part of the flux rope, these outlying fluxes should not be included. After  $dX$  and  $dY$  were determined,  $(dX \cdot dY)$ , which will be referred to as  $(dXdY)$  hereinafter, was used as a measure of area of the cross section of the emerging magnetic flux rope. The changing rate of all these parameters was computed by taking the time derivatives:  $V_X \equiv \partial dX/\partial t$ ,  $V_Y \equiv \partial dY/\partial t$ , and  $V_{XY} \equiv \partial(dXdY)/\partial t$ .

### 4.3. Vertical Motion

Schüssler (1979) was the first to derive an analytical expression for the magnetic buoyant force of a horizontal cylindrical magnetic tube with an arbitrary radius, under the simplification of constant temperature, uniform magnetic field, constant gravity, and constant pressure scale-height across the cross section, which is

$$\tilde{F}_B = \frac{1}{4} B_0^2 \cdot a \cdot \exp(-a/\Lambda) \cdot I_1(a/\Lambda), \quad (6)$$

where  $\tilde{F}_B$  is the magnetic buoyant force *per* unit length,  $a$  is the tube radius,  $B_0$  and  $\Lambda$  are the magnetic field and pressure scale-height of the cross section of the tube, and  $I_1$  is the modified Bessel function of order 1. In the limit of  $a/\Lambda \ll 1$  (thin flux-tube approximation) and of  $a/\Lambda \gg 1$  (thick flux-tube approximation),  $\tilde{F}_B$  simplifies to the following:

$$\tilde{F}_B \approx \frac{B_0^2 \cdot a^2}{8\Lambda} \quad (a/\Lambda \ll 1) \text{ and} \quad (7)$$

$$\tilde{F}_B \approx \frac{B_0^2}{4(2\pi)^{1/2}} (a \cdot \Lambda)^{1/2} \quad (a/\Lambda \gg 1). \quad (8)$$



Using Equations (7) and (8) and assuming that the upward buoyant force is balanced by a downward drag force of the following form:

$$\tilde{F}_d = \frac{1}{2}\rho_e v^2 C_d \cdot 2a, \quad (9)$$

where  $\tilde{F}_d$  is the drag force *per* unit length,  $\rho_e$  is the ambient gas density,  $v$  is the velocity, and  $C_d$  is drag coefficient, Chou and Wang (1987) derived the buoyant velocities for the thin and thick flux-tube approximations, as:

$$V_{\text{bn}} = V_A \left( \frac{\pi}{2C_d} \right)^{1/2} \left( \frac{a}{\Lambda} \right)^{1/2} \quad (a \ll \Lambda) \text{ and} \quad (10)$$

$$V_{\text{bk}} = V_A \left( \frac{\pi}{2C_d^2} \right)^{1/4} \left( \frac{\Lambda}{a} \right)^{1/4} \quad (a \gg \Lambda), \quad (11)$$

where  $V_A = B_0/\sqrt{4\pi\rho_e}$  is the Alfvén speed, and  $V_{\text{bn}}$  and  $V_{\text{bk}}$  denote the thin and thick flux-tube buoyant velocities, respectively. To derive the buoyant velocities at the surface layer, the parameters  $\rho_e$ ,  $\Lambda$  and  $C_d$  are set to their photospheric values:

$$\rho_e = 3.2 \times 10^{-7} \text{ g cm}^{-3}, \quad (12)$$

$$\Lambda = 200 \text{ km} = 2 \times 10^7 \text{ cm}, \quad (13)$$

$$C_d = 1 \text{ (dimensionless)}. \quad (14)$$

Equations (10) and (11) show that the buoyant velocities are mainly dependent on the magnetic field strength and radius of the flux tube, specifically,  $V_{\text{bn}} \propto B_0 a^{1/2}$  and  $V_{\text{bk}} \propto B_0 a^{-1/4}$ . Since our analysis is based on the hypothesis that the entire emerging active region is formed by a single flux tube, we used  $dY/2$  as a measure of the radius, and the magnetic field strength was set to be the average magnetic field of the emerging flux region.

As shown in Figures 7 and 8, a large portion of the area bounded by  $dX$  and  $dY$  have very weak magnetic field strength. To calculate a meaningful average magnetic field of the emerging flux region, the area with weak background field should not be included. To distinguish the emerging flux region from the background field, we applied a threshold to filter out weak-field regions, that is, the regions with  $|B|$  less than a threshold value,  $|B|_{\text{thr}}$ , were neglected. Because the field strength of the emerging flux changes significantly from the earliest stages of emergence to its maximum value, the threshold should not be fixed but should be adjusted according to the stage of the emergence. The threshold should be sufficiently high to exclude most of the noise but also sufficiently low such that the initial emerging fluxes are not overlooked. Since an emerging magnetic flux structure is expected to be more concentrated than the background field and should first appear at the photosphere as horizontal, the threshold  $|B|_{\text{thr}}$  was chosen to be the average field strength of the inclined fields within  $dX$  and  $dY$ . “Inclined” field in this study is defined as the field vector with inclination angle

$\theta_B$  between  $50^\circ$  and  $130^\circ$ , following the criteria in Centeno (2012). Therefore,

$$|B|_{\text{thr}} = \frac{\sum |B|^{\text{inclined}}}{N_{50^\circ < \theta_B < 130^\circ}}, \quad (15)$$

where  $\sum |B|^{\text{inclined}}$  is the sum of  $|B|$  of the inclined field vectors, and  $N_{50^\circ < \theta_B < 130^\circ}$  is the total number of pixels of the inclined fields. We point out that the inclination angle of the ME data is measured relative to LOS while that of the CEA data is measured relative to the radial direction. Therefore, if the projection effect needs to be considered, that is, if the LOS is far from the local vertical direction, the results of both should differ.

After the threshold was determined, the average field was calculated in two different ways: 1) averaging over all strong fields (*i.e.*,  $|B| > |B|_{\text{thr}}$ ):

$$\langle |B|^{\text{all}} \rangle = \frac{\sum_{|B| > |B|_{\text{thr}}} |B|}{N^{\text{all}}}, \quad (16)$$

and 2) averaging over the strong field where the field vector is inclined:

$$\langle |B|^{\text{inclined}} \rangle = \frac{\sum_{|B|^{\text{inclined}} > |B|_{\text{thr}}} |B|^{\text{inclined}}}{N^{\text{inclined}}}, \quad (17)$$

where  $N^{\text{all}} \equiv N_{|B| > |B|_{\text{thr}}}$  is the total number of pixels with strong field values, and  $N^{\text{inclined}} \equiv N_{|B|^{\text{inclined}} > |B|_{\text{thr}}}$  is the total number of pixels with strong field values for which the field vector is inclined. Note that the difference  $N^{\text{all}} - N^{\text{inclined}}$  is simply the number of pixels with strong fields and vertically oriented field vectors. For the rest of this article, the average field and associated quantities of the former will be referred to as ‘‘all-direction’’ and labeled with the superscript ‘‘all’’, while those of the latter will be referred to as ‘‘inclined-field’’ and labeled with the superscript ‘‘inclined’’.

The results using ME and CEA data after filtering are shown in Figure 9 and Figure 10, respectively. The plotted regions are inside the white boxes shown in Figures 7 and 8. The fields lower than  $|B|_{\text{thr}}$  were set to zero (blue). The regions with non-zero values and inclined fields are shown in white to distinguish them from the regions with more vertically oriented field. Comparing Figures 7 and 8 with Figures 9 and 10, we find that the first four images are still very noisy after the filtering, indicating that  $|B|_{\text{thr}}$  during the early stage of the flux emergence is comparable to the noise level, causing some stronger random noise to be included as part of the emerging flux region. However, since the only relevant output from this filtering process is the average total-field strength, such imperfect filtering should not introduce significant errors to  $\langle |B|^{\text{all}} \rangle$  and  $\langle |B|^{\text{inclined}} \rangle$  and the subsequently computed  $V_{\text{bk}}$  and  $V_{\text{bn}}$ , as long as the field strength of the included noise is similar to that in the emerging flux region. Our second observation is that the field vectors were predominantly inclined during the early stage of emergence, but became more vertically oriented later. This is consistent with the expected characteristics of a magnetic flux tube rising through the photosphere, and has been widely reported in both observations and theoretical models (*e.g.*, Chou and Fisher, 1989; Chou, 1993; Caligari, Moreno-Insertis, and Schüssler,

1995; Lites, Skumanich, and Martinez Pillet, 1998; Fan, 2004; Centeno, 2012). Our third observation is that the two polarities were connected by inclined fields during most of the emerging process, but gradually they broke up to become two separated regions, each of which is surrounded by a ring of inclined fields (*cf.* last row of Figure 10). These observations are consistent with general properties of emerging active regions.

After  $\langle |B|^{\text{all}} \rangle$  and  $\langle |B|^{\text{inclined}} \rangle$  were determined, we used  $dY/2$  as a proxy for the flux tube radius and derived the buoyant velocities for thick and thin flux-tube approximation (*i.e.*,  $V_{\text{bk}}$  and  $V_{\text{bn}}$ ). We also computed the changing rates of  $\langle |B|^{\text{all}} \rangle$ ,  $\langle |B|^{\text{inclined}} \rangle$ ,  $V_{\text{bk}}$ , and  $V_{\text{bn}}$ .

## 5. Results and Discussion

The temporal profiles of the total unsigned flux in the entire region cut from HMI full-disk magnetograms are plotted in Figure 11 to show how the total flux was changing during the flux emergence. The upper panel shows the results computed from the original ME (black) and CEA (red) data without any filtering. The lower panel shows the results of the filtered data, that is, only  $|B| > |B|_{\text{thr}}$  was included in the summation. Both plots show that the total flux began to increase around 2 January 2013 at 16:00 UT. The main emergence lasted for approximately 16 hours until around 3 January 2013 at 08:00 UT, after which the increasing rate became lower. Comparison between the two plots shows that the unfiltered results contain two spikes (at  $\approx 01:00$  UT and  $18:00$  UT on 3 January 2013) and a gap between the ME and CEA profiles. Both disappeared in the filtered result in the lower panel. This indicates that both features are likely caused by the weak-field noise.

In Figure 12, the quantities associated with the horizontal motion ( $dX$ ,  $dY$ ,  $dXdY$ ), and their temporal derivatives) of the EAR are plotted in the upper two rows and those associated with the vertical motion ( $\langle |B|^{\text{all}} \rangle$ ,  $\langle |B|^{\text{inclined}} \rangle$ ,  $V_{\text{bk}}$ ,  $V_{\text{bn}}$ , and their temporal derivatives) in the lower two. The plots in the upper two rows show that the horizontal motion determined from ME (black) and CEA (red) data are consistent with each other. The time profiles of  $dX$  and  $V_X$  show that the separation of the two polarities was fastest ( $\approx 4.0$  Mm hr $^{-1}$ ) during the initial emergence, as indicated by the steep slope in  $dX$  *vs.* time and the peak in  $V_X$  *vs.* time at  $\approx 16:00$  UT on 2 January 2013. The two polarities continued to separate at a lower speed afterward. The two plateaus in  $V_X$  *vs.* time indicate that the separation speed decreased twice,  $\approx 3$  Mm hr $^{-1}$  at around 01:00 UT on 3 January 2013 and  $\approx 1$  Mm hr $^{-1}$  at around 11:00 UT on 3 January 2013. Our result is qualitatively similar to those found in earlier studies (*e.g.*, Harvey and Martin, 1973; Chou and Wang, 1987; Strous *et al.*, 1996; Shimizu *et al.*, 2002), which showed that the separation of the opposite polarities is fastest at the beginning of the emergence but becomes slower later. The exact values of the separation speeds, however, differ among different studies.

The extension,  $dY$ , did not begin to increase until after  $\approx 18:00$  UT on 2 January 2013, and reached its peak rate of  $\approx 4.0$  Mm hr $^{-1}$  in about three hours at  $\approx 21:00$  UT on 2 January 2013. The increase of  $dY$  began to slow down

after  $\approx 23:00$  UT on 2 January 2013, and stayed at an almost constant rate of  $\approx 1 \text{ Mm hr}^{-1}$  at the end of our observation. It is interesting to note that while  $V_X$  and  $V_Y$  seem to be anticorrelated at the initial emerging phase, the two have similar peak and terminal speeds. One possible explanation is that the peak and terminal speeds of both extension and separation may simply depend on the total strength and dissipation of the emerging magnetic flux tube, while the detailed temporal profile of the motion in the two directions may be influenced by more complex factors, such as surface flows, turbulence, and others.

The third row shows that the average fields and buoyant velocities derived from ME and CEA data differ, with the CEA results (red) lower than the ME results (black). The difference is especially prominent in  $V_{\text{bn}}$  vs. time. Comparing the all-direction (higher) and inclined-field (lower) curves in this row, it can be seen that the two were almost the same at the beginning of the emergence, and deviated from each other later. The gap between the two widened as  $\langle |B|^{\text{all}} \rangle$ ,  $\langle |B|^{\text{inclined}} \rangle$ ,  $V_{\text{bk}}$ , and  $V_{\text{bn}}$  increased, and gradually became nearly a constant after these four quantities reached their respective peaks. These curves are qualitatively consistent with the image sequence in Figures 9 and 10. It can also be noticed that the all-direction curves peaked slightly later than the inclined-field curves in all three panels. The plot of  $V_{\text{bn}}$  reveals that the buoyant velocity of the thin flux-tube approximation is about 20 times larger than the horizontal velocity  $V_X$  and  $V_Y$ , indicating that the thin flux-tube approximation is inappropriate. The peak  $V_{\text{bk}}$  is slightly smaller than the peak in  $V_X$  and  $V_Y$ , but the three speeds are generally of similar magnitudes.

Centeno (2012) examined the relationship between the inclination angles and the Doppler velocities of all points in two emerging active regions that emerged in a free field environment. The scatter plots in the paper showed that the inclined-field areas had an upward velocity of  $\leq 400 \text{ m s}^{-1}$  ( $\approx 1.5 \text{ Mm hr}^{-1}$ ), which is similar to our computed  $V_{\text{bk}}^{\text{inclined}}$  based on the buoyancy theory.

Lites, Skumanich, and Martinez Pillet (1998) reported a higher upward Doppler velocity of  $\approx 1 \text{ km s}^{-1}$  for horizontal magnetic elements. However, at least one of the regions selected by Lites, Skumanich, and Martinez Pillet (1998) was located within some preexisting magnetic field, which may have affected the rising motion of the emerging flux.

An early study by Chou and Wang (1987), which used LOS magnetograms, reported a thick flux-tube buoyant velocity that was much larger than the separation velocity. LOS magnetograms mainly detect the vertically oriented fields, which usually have stronger field strength and occur in the later stage of the flux emergence than the horizontally oriented fields (*e.g.*, Kubo, Shimizu, and Lites, 2003). As revealed in our analysis, the separation of the two polarities quickly slowed down to less than  $1 \text{ Mm hr}^{-1}$  after  $\langle |B|^{\text{inclined}} \rangle$  and  $\langle |B|^{\text{all}} \rangle$  reached their maximum. In contrast, the buoyant velocities remain  $\geq 1 \text{ Mm hr}^{-1}$  at the last point of our observation.

In the last row of Figure 12, we plotted the temporal derivatives of  $\langle |B|^{\text{all}} \rangle$ ,  $\langle |B|^{\text{inclined}} \rangle$ ,  $V_{\text{bk}}^{\text{all}}$ ,  $V_{\text{bk}}^{\text{inclined}}$ ,  $V_{\text{bn}}^{\text{all}}$ , and  $V_{\text{bn}}^{\text{inclined}}$ . Despite the difference between the all-direction and inclined-field quantities in the third row, their temporal derivatives overlap, and have a similar decreasing profiles. In other words, the changing rates of all these quantities are similar.

Next, we examined how the percentage of the inclined field in the EAR evolves during the emerging process. In Figure 13, we plotted the time profiles of the ratio  $\langle |B|^{\text{inclined}} \rangle / \langle |B|^{\text{all}} \rangle$  in the upper panel, and the ratio of the occupied area  $N^{\text{inclined}} / N^{\text{all}}$  in the lower panel. The two profiles show a similar decreasing trend, both began at  $\approx 1$  and decreased to a terminal value of  $\approx 0.6 - 0.7$ . Comparing this figure with the third row of Figure 12, we can see that the ratios decreased as  $\langle |B|^{\text{all}} \rangle$  and  $\langle |B|^{\text{inclined}} \rangle$  increased, and reached the terminal value at approximately the same time as when  $\langle |B|^{\text{all}} \rangle$  and  $\langle |B|^{\text{inclined}} \rangle$  reached their peaks (at  $\approx 06:00$  UT on 3 January 2013).

To understand the plots, we rewrite  $\langle |B|^{\text{inclined}} \rangle / \langle |B|^{\text{all}} \rangle$  as follows:

$$\frac{\langle |B|^{\text{inclined}} \rangle}{\langle |B|^{\text{all}} \rangle} = \frac{\sum |B|^{\text{inclined}} / \sum |B|^{\text{all}}}{N^{\text{inclined}} / N^{\text{all}}}. \quad (18)$$

Since  $N^{\text{inclined}} \approx N^{\text{all}}$  at the beginning of the emergence, as revealed in Figure 9,  $\sum |B|^{\text{all}}$  must be almost equal to  $\sum |B|^{\text{inclined}}$  during the initial stage of the flux emergence, indicating that the proportion of vertically oriented fields during this time is very small or almost negligible. After  $\langle |B|^{\text{all}} \rangle$  and  $\langle |B|^{\text{inclined}} \rangle$  reached their maximum, Figure 13 shows that  $\langle |B|^{\text{inclined}} \rangle / \langle |B|^{\text{all}} \rangle$  and  $N^{\text{inclined}} / N^{\text{all}}$  both became approximately 0.6, leading to  $\sum |B|^{\text{inclined}} / \sum |B|^{\text{all}} \approx 0.36$  according to Equation (18). In other words, while the inclined fields still cover a larger percentage of the area (60%), as qualitatively shown in the last row of Figure 9, the sum of the inclined fields becomes only 36% of the sum of all-direction fields. Since  $\sum |B|^{\text{all}} = \sum |B|^{\text{inclined}} + \sum |B|^{\text{vertical}}$  and  $N^{\text{all}} = N^{\text{inclined}} + N^{\text{vertical}}$ , we can deduce that  $\sum |B|^{\text{vertical}} / \sum |B|^{\text{all}} \approx 0.64$ ,  $N^{\text{vertical}} / N^{\text{all}} \approx 0.4$  and  $\langle |B|^{\text{vertical}} \rangle / \langle |B|^{\text{all}} \rangle \approx 1.6$ , indicating that the vertically oriented fields became very concentrated in an area about 40% of the EAR after the growing phase of the emergence.

Finally, we examined the relationship between the horizontal and vertical motions. In Figure 14, the three horizontal speeds,  $V_X$ ,  $V_Y$ , and  $V_{XY}$ , are plotted *vs.*  $V_{\text{bk}}^{\text{all}}$  (left) and  $V_{\text{bk}}^{\text{inclined}}$  (right) in the upper three rows. The last row shows  $\langle |B|^{\text{all}} \rangle$  *vs.*  $V_{\text{bk}}^{\text{all}}$  (left) and  $\langle |B|^{\text{inclined}} \rangle$  *vs.*  $V_{\text{bk}}^{\text{inclined}}$  (right). In all plots, the individual edge-tracing results of the ME data are plotted in black triangles and those of the CEA data in red crosses. The averages of the individual tracing results are connected by thick lines to guide the eyes. To distinguish the increasing and decreasing phases of  $\langle |B|^{\text{all}} \rangle$  and  $\langle |B|^{\text{inclined}} \rangle$ , the thick lines corresponding to the two phases are plotted in different colors. The growing and decaying phases of the ME results are plotted in black and blue, respectively. Those of the CEA results are plotted in red and orange, respectively. From the plots in the upper three rows, we did not find a correlation or dependence between the horizontal motion and the buoyant motion. While the data points are not randomly scattered, the horizontal and buoyant speeds seem to evolve independently of each other. The last row, in contrast, shows a clear positive correlation between  $\langle |B| \rangle$  and  $V_{\text{bk}}$ . The slopes of the growing and decaying phases are slightly different.

Since we found in Figures 12 and 13 that the temporal derivatives of the average field and buoyant velocities and the ratio  $\langle |B|^{\text{inclined}} \rangle / \langle |B|^{\text{all}} \rangle$  all decrease with time as  $V_X$  does, we investigated whether any correlation may exist

among them. In Figure 15,  $V_X$  was plotted against  $d\langle|B|\rangle/dt$  in the top row,  $\langle|B|^{\text{inclined}}\rangle/\langle|B|^{\text{all}}\rangle$  in the middle row, and  $dV_{\text{bk}}/dt$  in the bottom row.  $d\langle|B|\rangle/dt$  is a notation to represent  $d\langle|B|^{\text{all}}\rangle/dt$  and  $d\langle|B|^{\text{inclined}}\rangle/dt$ , and  $dV_{\text{bk}}/dt$  represents  $dV_{\text{bk}}^{\text{all}}/dt$  and  $dV_{\text{bk}}^{\text{inclined}}/dt$ . The results from ME and CEA data are in the left and right columns, respectively. In the top and bottom rows, the inclined-field results are represented by red crosses, and the all-direction results by black triangles. Some positive linear correlations are visible in most of the plots, especially in those in the right column. To quantify the level of the correlation, we calculated and showed the correlation coefficients (CCs) in the corresponding panels. The results show that most of the correlation coefficients are higher than 0.5, indicating the existence of some positive correlation. The correlation is stronger in the CEA data than in the ME data. As described in Section 2, the CEA data do not include the earliest stage of flux emergence when the flux is weak and can be contaminated by noise, and the fields have been properly decomposed into radial and horizontal components. These facts can reduce the errors in the determination of  $\langle|B|^{\text{inclined}}\rangle$ ,  $\langle|B|^{\text{all}}\rangle$ ,  $dX$ , and  $dY$ , and lead to the better correlation found in the CEA results. The correlation coefficient also reveals that the correlation is stronger for the all-direction quantities than for the inclined-field quantities. The inclined fields were thought to be the top of emerging flux tube. While the weaker magnitude and larger observational errors of the inclined field may partly contribute to the lower correlation, it can also indicate that the simplistic assumption of a single flux tube rising through the photosphere may not be appropriate.

## 6. Summary

In this study, we compared the observed horizontal motion and the theoretically derived vertical motion of an emerging active region to test the assumption that it can be represented by the intersection of a rising magnetic tube, whose dynamics is mainly governed by the magnetic buoyancy mechanism and whose structure can be considered rigid or not significantly distorted by surface and near-surface effects, as it crosses the solar surface.

The selected target is AR 11645. We tracked this AR emergence from the earliest detectable appearance of magnetic flux at  $\approx 14:00$  UT on 2 January 2013 until 23:59:59 UT on 3 January 2013. In this period of time, the average field strength reached its peak at  $\approx 06:00$  UT on 3 January 2013. The region of emergence was initially free of preexisting field, and was not associated with any eruption during the flux emergence process. At the early stage, many small and transient flux concentrations rapidly emerged with seemingly arbitrary polarity orientations, and later organized in an East-West direction to form a bipolar configuration. Chou (1993) argued that this is an indication that the EAR is not significantly affected by local surface effects.

Our analysis of the horizontal motion showed that the separation of the two polarities of this region was fastest ( $V_X \approx 4.0$  Mm hr $^{-1}$ ) at the beginning, slowed down as the emergence continued, and reached a near constant speed of  $\leq 1$  Mm hr $^{-1}$  after  $\langle|B|^{\text{all}}\rangle$  and  $\langle|B|^{\text{inclined}}\rangle$  reached their peaks. The extension of

the region in the direction perpendicular to the line connecting the two poles did not begin until  $\approx 4$  hours after the first sign of flux emergence, reached its peak velocity ( $V_Y \approx 4.0 \text{ Mm hr}^{-1}$ ) approximately three hours later, and decreased to  $\approx 1 \text{ Mm hr}^{-1}$  at the end of the observation time.

To investigate the vertical motion, we used the buoyant velocities of thin and thick flux-tube approximations derived by Chou and Wang (1987), and considered  $dY/2$  as the flux-tube radius and the average  $|B|$  of the EAR as the field strength of the flux tube. The computed buoyant velocities revealed that the thin flux-tube approximation is inappropriate because it results in an unreasonably high buoyant speed. The thick flux-tube buoyant velocity of the inclined field vectors has a similar magnitude as the the horizontal velocity of this EAR, and is also consistent with the Doppler velocity of inclined fields reported by Centeno (2012). This indicates that the magnetic buoyancy mechanism is valid and that the emergence was largely governed by it.

The temporal profiles of the average field strength and buoyant velocity show a growing and a decaying phase, and are positively correlated. However, they do not show a dependence or correlation with the observed horizontal motion. The uncorrelation between the horizontal and vertical motions suggests that the assumption that EARs are formed by the emergence of flux tubes whose structures remain constant as they cross the surface should be taken with caution.

However, some positive correlations are found between the separation velocity  $V_X$  and  $d\langle|B|^{\text{all}}\rangle/dt$ ,  $dV_{\text{bk}}^{\text{all}}/dt$ , and  $\langle|B|^{\text{inclined}}\rangle/\langle|B|^{\text{all}}\rangle$ . This indicates that the separation speed of the two polarities can be related to the percentage of the inclined fields, and the increase rate of the average field and buoyant speed. Whether or not this relationship is a general property for emerging active regions would require more case studies.

**Acknowledgments** This work is funded by the MOST of ROC under grant NSC 102-2112-M-008-018 and the MOE grant ‘‘Aim for the Top University’’ to the National Central University.

#### Disclosure of Potential Conflicts of Interest

The authors declare that they have no conflicts of interest.

## References

- Brandenburg, A., Kemel, K., Kleorin, N., Mitra, D., Rogachevskii, I.: 2011, Detection of Negative Effective Magnetic Pressure Instability in Turbulence Simulations. *Astrophys. J. Lett.* **740**, L50. DOI. ADS. [Brandenburg2011ApJ]
- Calabretta, M.R., Greisen, E.W.: 2002, Representations of celestial coordinates in FITS. *Astron. Astrophys.* **395**, 1077. DOI. ADS. [CalabrettaGreisen2002AA]
- Caligari, P., Moreno-Insertis, F., Schüssler, M.: 1995, Emerging flux tubes in the solar convection zone. 1: Asymmetry, tilt, and emergence latitude. *Astrophys. J.* **441**, 886. DOI. ADS. [Caligari\_etal1995ApJ]
- Centeno, R.: 2012, The Naked Emergence of Solar Active Regions Observed with SDO/HMI. *Astrophys. J.* **759**, 72. DOI. ADS. [centeno2012ApJ]
- Cheung, M.C.M., Isobe, H.: 2014, Flux Emergence (Theory). *Living Rev. in Solar Phys.* **11**, 3. DOI. ADS. [CI2014LRSP]
- Chintzoglou, G., Zhang, J.: 2013, Reconstructing the Subsurface Three-dimensional Magnetic Structure of a Solar Active Region Using SDO/HMI Observations. *Astrophys. J. Lett.* **764**, L3. DOI. ADS. [CZ2013ApJ]

- Chou, D.-Y.: 1993, Structure of emerging flux regions. In: Zirin, H., Ai, G., Wang, H. (eds.) *IAU Colloq. 141: The Magnetic and Velocity Fields of Solar Active Regions*, *Astron. Soc. Pacific C. S.* **46**, 471. ADS. [chou1993ASPC]
- Chou, D.-Y., Fisher, G.H.: 1989, Dynamics of anchored flux tubes in the convection zone. I - Details of the model. *Astrophys. J.* **341**, 533. DOI. ADS. [CF1989ApJ]
- Chou, D.-Y., Wang, H.: 1987, The separation velocity of emerging magnetic flux. *Solar Phys.* **110**, 81. DOI. ADS. [CW1987SoPh]
- Fan, Y.: 2004, Dynamics of Emerging Flux Tubes. In: Sakurai, T., Sekii, T. (eds.) *The Solar-B Mission and the Forefront of Solar Physics*, *Astron. Soc. Pacific C. S.* **325**, 47. ADS. [Fan2004ASPC]
- Fan, Y.: 2008, The Three-dimensional Evolution of Buoyant Magnetic Flux Tubes in a Model Solar Convective Envelope. *Astrophys. J.* **676**, 680. DOI. ADS. [Fan2008ApJ]
- Harvey, K.L., Martin, S.F.: 1973, Ephemeral Active Regions. *Solar Phys.* **32**, 389. DOI. ADS. [HM1973SoPh]
- Hoeksema, J.T., Liu, Y., Hayashi, K., Sun, X., Schou, J., Couvidat, S., Norton, A., Bobra, M., Centeno, R., Leka, K.D., Barnes, G., Turmon, M.: 2014, The Helioseismic and Magnetic Imager (HMI) Vector Magnetic Field Pipeline: Overview and Performance. *Solar Phys.* **289**, 3483. DOI. ADS. [HMI\_ME2014SoPh289]
- Kubo, M., Shimizu, T., Lites, B.W.: 2003, The Evolution of Vector Magnetic Fields in an Emerging Flux Region. *Astrophys. J.* **595**, 465. DOI. ADS. [ks12003ApJ]
- Leka, K.D., Canfield, R.C., McClymont, A.N., van Driel-Gesztelyi, L.: 1996, Evidence for Current-carrying Emerging Flux. *Astrophys. J.* **462**, 547. DOI. ADS. [Leka\_etal1996ApJ]
- Lites, B.W., Skumanich, A., Martinez Pillet, V.: 1998, Vector magnetic fields of emerging solar flux. I. Properties at the site of emergence. *Astron. Astrophys.* **333**, 1053. ADS. [lsm1998AA]
- Metcalf, T.R.: 1994, Resolving the 180-degree ambiguity in vector magnetic field measurements: The 'minimum' energy solution. *Solar Phys.* **155**, 235. DOI. ADS. [Metcalf1994SoPh]
- Parker, E.N.: 1955, The Formation of Sunspots from the Solar Toroidal Field. *Astrophys. J.* **121**, 491. DOI. ADS. [parker1955ApJ121]
- Parker, E.N.: 1978, Hydraulic concentration of magnetic fields in the solar photosphere. VI - Adiabatic cooling and concentration in downdrafts. *Astrophys. J.* **221**, 368. DOI. ADS. [parker1978ApJ]
- Pesnell, W.D., Thompson, B.J., Chamberlin, P.C.: 2012, The Solar Dynamics Observatory (SDO). *Solar Phys.* **275**, 3. DOI. ADS. [SD0\_2012SoPh275]
- Rempel, M.: 2011, Subsurface Magnetic Field and Flow Structure of Simulated Sunspots. *Astrophys. J.* **740**, 15. DOI. ADS. [Rempel2011ApJ]
- Rempel, M., Cheung, M.C.M.: 2014, Numerical Simulations of Active Region Scale Flux Emergence: From Spot Formation to Decay. *Astrophys. J.* **785**, 90. DOI. ADS. [RempelCheung2014ApJ]
- Schou, J., Scherrer, P.H., Bush, R.I., Wachter, R., Couvidat, S., Rabello-Soares, M.C., Bogart, R.S., Hoeksema, J.T., Liu, Y., Duvall, T.L., Akin, D.J., Allard, B.A., Miles, J.W., Rairden, R., Shine, R.A., Tarbell, T.D., Title, A.M., Wolfson, C.J., Elmore, D.F., Norton, A.A., Tomczyk, S.: 2012, Design and Ground Calibration of the Helioseismic and Magnetic Imager (HMI) Instrument on the Solar Dynamics Observatory (SDO). *Solar Phys.* **275**, 229. DOI. ADS. [HMI\_2012SoPh275]
- Schüssler, M.: 1979, Magnetic buoyancy revisited - Analytical and numerical results for rising flux tubes. *Astron. Astrophys.* **71**, 79. ADS. [Schuessler1979AA]
- Shimizu, T., Shine, R.A., Title, A.M., Tarbell, T.D., Frank, Z.: 2002, Photospheric Magnetic Activities Responsible for Soft X-Ray Pointlike Microflares. I. Identifications of Associated Photospheric/Chromospheric Activities. *Astrophys. J.* **574**, 1074. DOI. ADS. [shimizu\_etal2002ApJ]
- Strous, L.H., Scharmer, G., Tarbell, T.D., Title, A.M., Zwaan, C.: 1996, Phenomena in an emerging active region. I. Horizontal dynamics. *Astron. Astrophys.* **306**, 947. ADS. [strous\_etal1996AA]
- Sun, X.: 2013, On the Coordinate System of Space-Weather HMI Active Region Patches (SHARPs): A Technical Note. *ArXiv e-prints*. ADS. [Sun2013arXiv]
- Tanaka, K.: 1991, Studies on a very flare-active delta group - Peculiar delta spot evolution and inferred subsurface magnetic rope structure. *Solar Phys.* **136**, 133. DOI. ADS. [Tanaka1991SoPh]



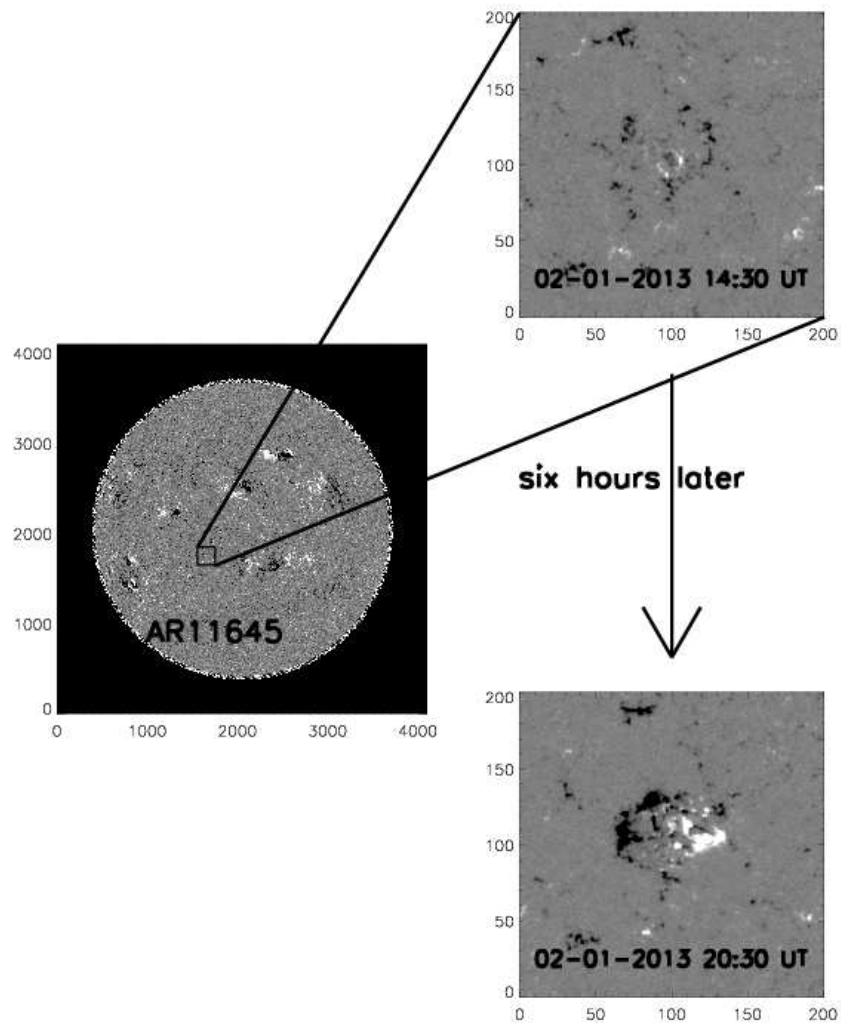


**Figure 1.** Emergence of AR11645 observed by SDO HMI line-of-sight magnetogram

Weber, M.A., Fan, Y., Miesch, M.S.: 2011, The Rise of Active Region Flux Tubes in the Turbulent Solar Convective Envelope. *Astrophys. J.* **741**, 11. DOI. ADS. [Weber\_etal2011ApJ]

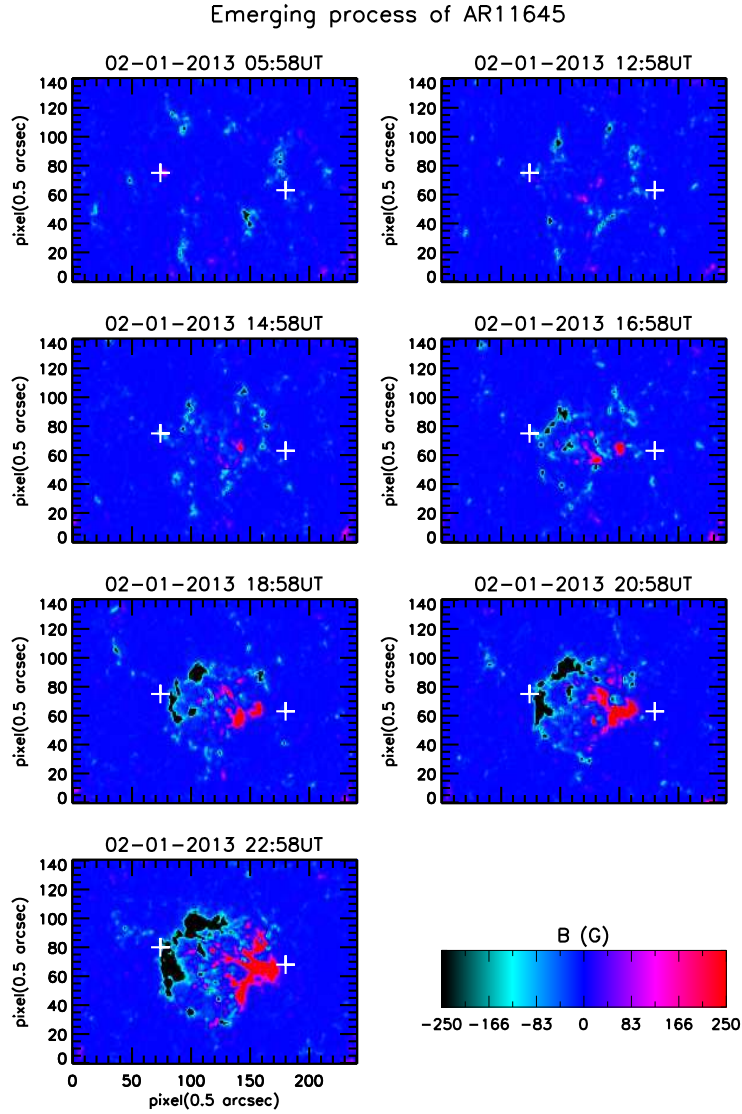


**Figure 2.** Selected HMI magnetogram cuts to show the emergence of AR11645. The observation times are indicated above the corresponding images. The size of a pixel in both X and Y directions is 0.05 arcsec. The two white crosses mark the approximate locations of the centers of the two polarities when the average total-field strength of the whole emerging active region reaches its maximum. The plotted quantity is the line-of-sight component of magnetic field, instead of the total field, such that the two polarities can be distinguished.

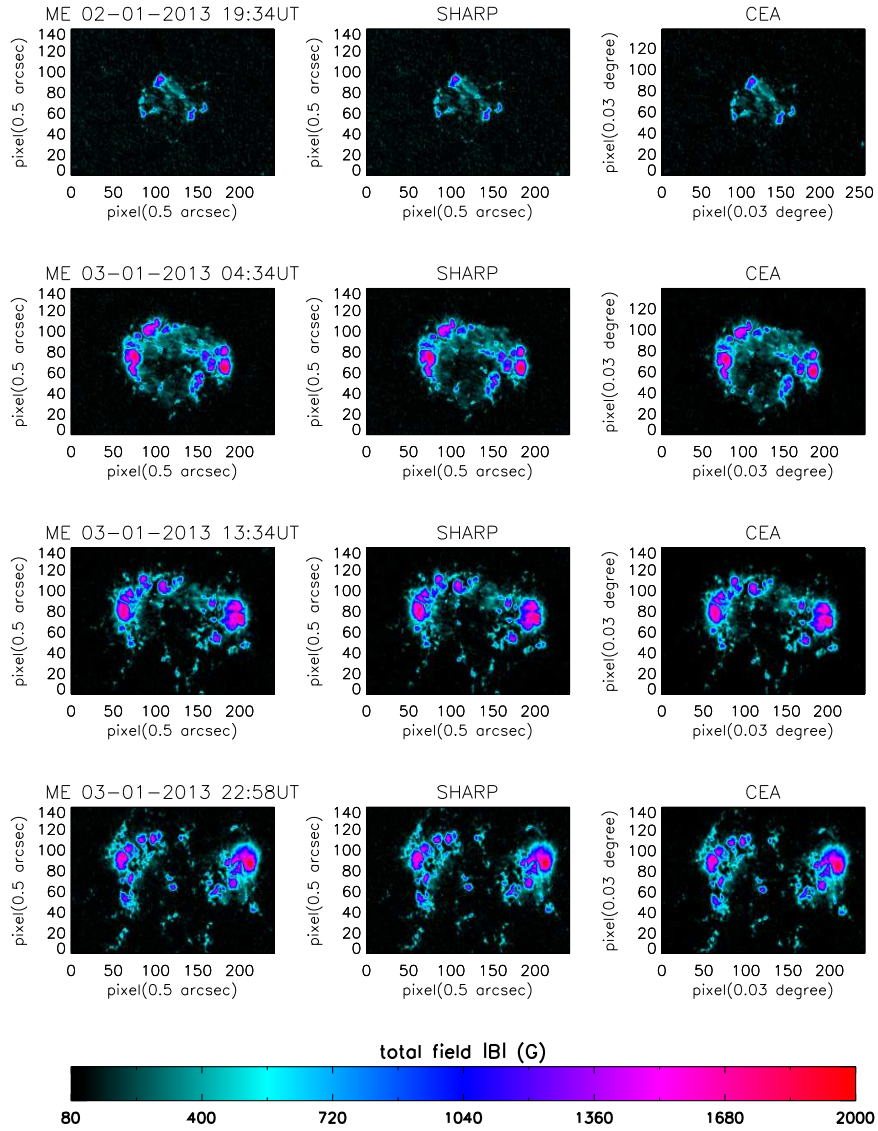


**Figure 3.** Selected total field ( $|B|$ ) images to illustrate the accuracy of the alignment between the cuts from HMI full-disk vector magnetograms (ME, left column), the Spaceweather HMI Active Region Patches (SHARP; middle), and the Cylindrical Equal Area mapped patches (CEA; right). The images in the same row correspond to the same observation time, which is indicated above the left panel. The length of each pixel of ME and SHARP is 0.5 arcsec, and that of CEA is  $0.03^\circ$ , as indicated along respective axis.

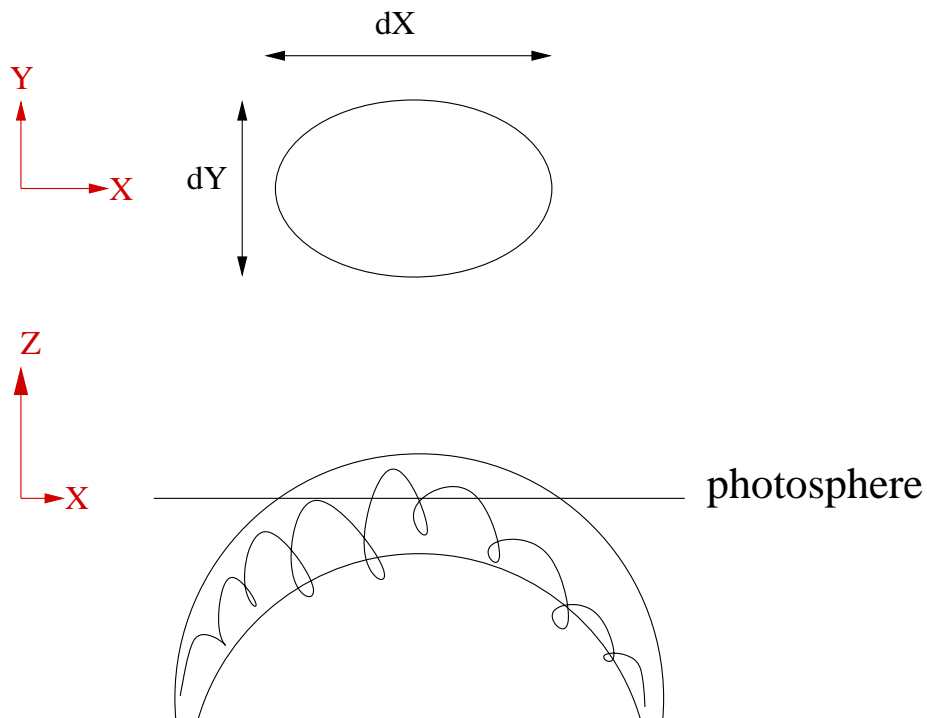


**Figure 4.** A cartoon illustrating the intersection of an emerging flux rope with the photosphere, which is represented by the horizontal line in the lower plot.  $dX$  represents the length of the cross section of the emerged flux rope, and corresponds to the separation of the two polarities.  $dY$  represents the width of the cross section, and corresponds to the extension of the emerging flux region.

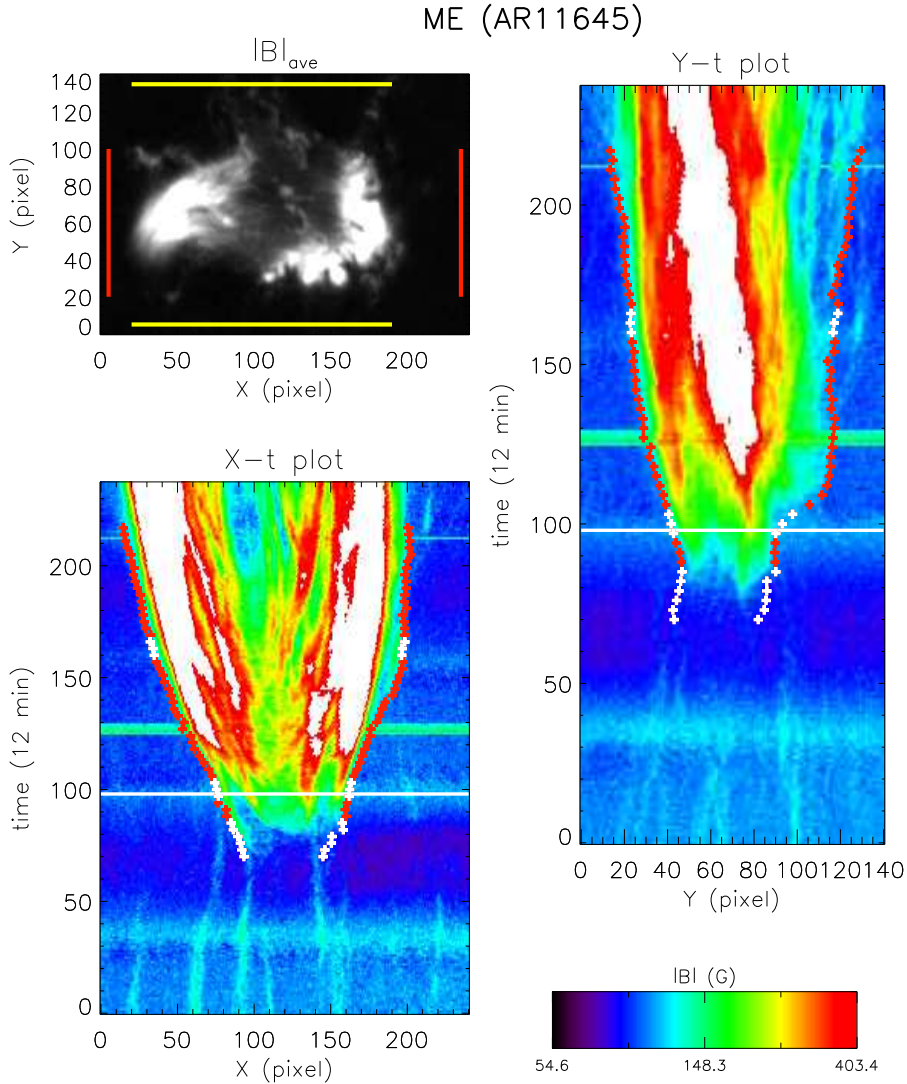


**Figure 5.** Upper left, lower left, and upper right panels are  $|B|_{\text{ave}}$ , X-t and Y-t plots created by averaging the total field data cube,  $|B|(X, Y, t)$ , over  $t$ ,  $Y$  and  $X$  dimensions, respectively. The red vertical and yellow horizontal lines in the upper left panel indicate the ranges over which the averages are done in  $Y$  and in  $X$ , respectively. The average range in  $t$  is the entire observation time. The data cube is the HMI full-disk vector magnetogram product ME. Due to a combination of satellite and instrument roll angles,  $|B|_{\text{ave}}$  is rotated  $180^\circ$  with respect to the real image, and the left and right of the X-t and Y-t plots are switched so that left should be right and *vice versa*. In both X-t and Y-t plots, the vertical direction is time (12 min *per* pixel), and the horizontal direction is length (0.5 arcsec *per* pixel). The magnitude of the total field in the X-t and Y-t plots is shown in the color bar in the lower right corner. The white regions in the X-t and Y-t plots are the regions with field strength higher than our plotting maximum 403.4 G.  $|B|_{\text{ave}}$  in the top left panel provides an overall idea of the emerging active region, and therefore the exact field strength is not shown. The red and white thick crosses in the X-t and Y-t plots are the manually traced edges of the emerging flux region (see the text for the difference between them). The white horizontal line marks the starting point of the HMI Active Region Patch data product (SHARP and CEA).

## CEA (AR11645)

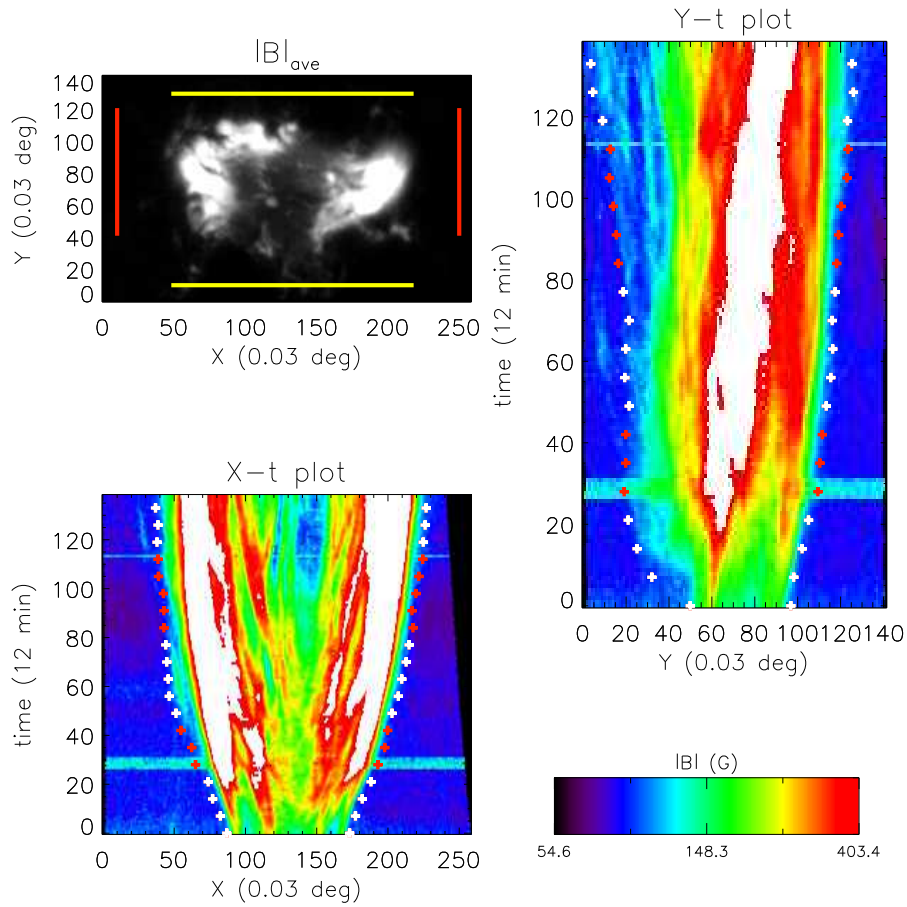


**Figure 6.** Upper left, lower left, and upper right panels are  $|B|_{\text{ave}}$ , X-t and Y-t plots created by averaging the total field data cube,  $|B|(X, Y, t)$ , over  $t$ ,  $Y$  and  $X$  dimensions, respectively. The red vertical and yellow horizontal lines in the upper left panel indicate the ranges over which the averages are done in  $Y$  and in  $X$ , respectively. The average range in  $t$  is the entire observation time. The data cube is the HMI Active Region Patch product CEA, and the plots are in the same orientation as the real image. In both X-t and Y-t plots, the vertical direction is time (12 min *per* pixel), and the horizontal direction is length (0.03° *per* pixel). The magnitude of the total field in the X-t and Y-t plots is shown in the color bar in the lower right corner. The white regions in the X-t and Y-t plots are the regions with field strength higher than our plotting maximum 403.4 G.  $|B|_{\text{ave}}$  in the top left panel provides an overall idea of the emerging active region, and therefore the exact field strength is not shown. The red and white thick crosses in the X-t and Y-t plots are the manually traced edges of the emerging flux region (see the text for the difference between them).

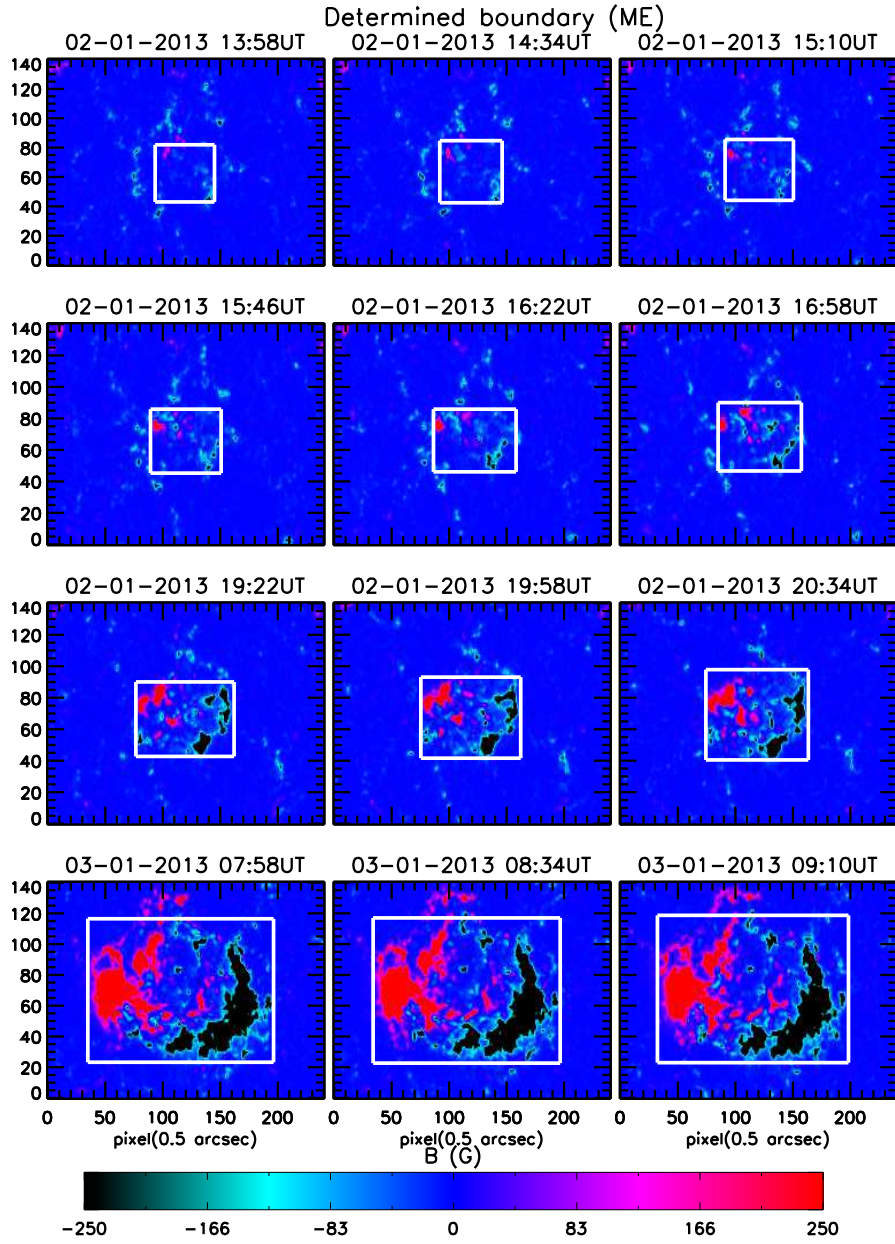


**Figure 7.** Selected images to check the accuracy of the EAR boundaries determined from the X-t and Y-t plots of the HMI vector magnetogram product ME (see Figure 5). The images plotted here correspond to the white crosses in Figure 5. The white boxes in each panel are the determined boundaries. The exact observation time is indicated above each panel. The pixel size in both X and Y directions is 0.5 arcsec, as indicated in the X-axis labels of the bottom row. We show the line-of-sight component of the field, instead of the total field, to distinguish the two polarities

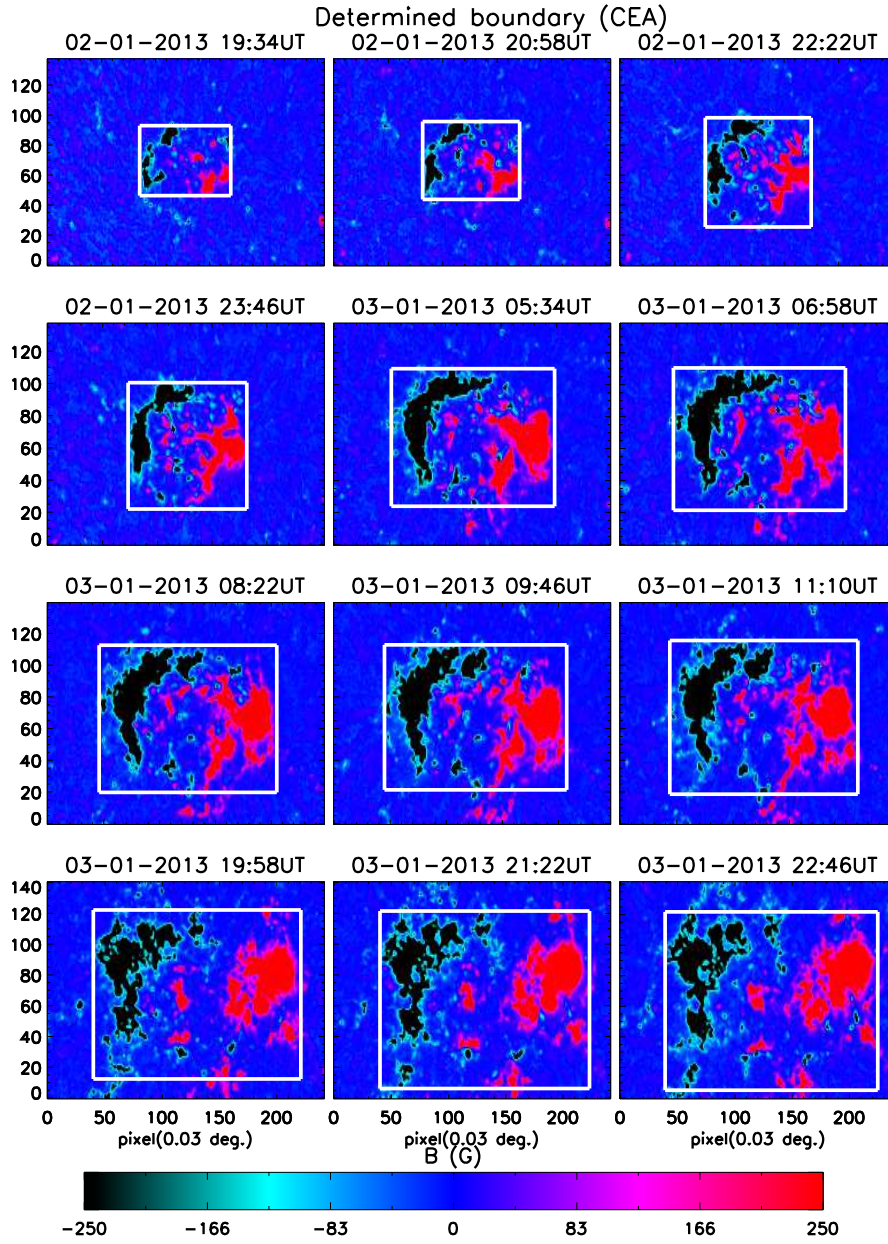


**Figure 8.** Selected images to check the accuracy of the EAR boundaries determined from the X-t and Y-t plots of the HMI vector magnetogram product CEA (see Figure 6). The images plotted here correspond to the white crosses in Figure 6. The white boxes in each panel indicate the determined boundaries. The observation time is indicated above each panel. The pixel size in both X and Y direction is 0.03 degree, as indicated in the X-axis labels of the last row. We show the radial component of the field, instead of the total field, to distinguish the two polarities



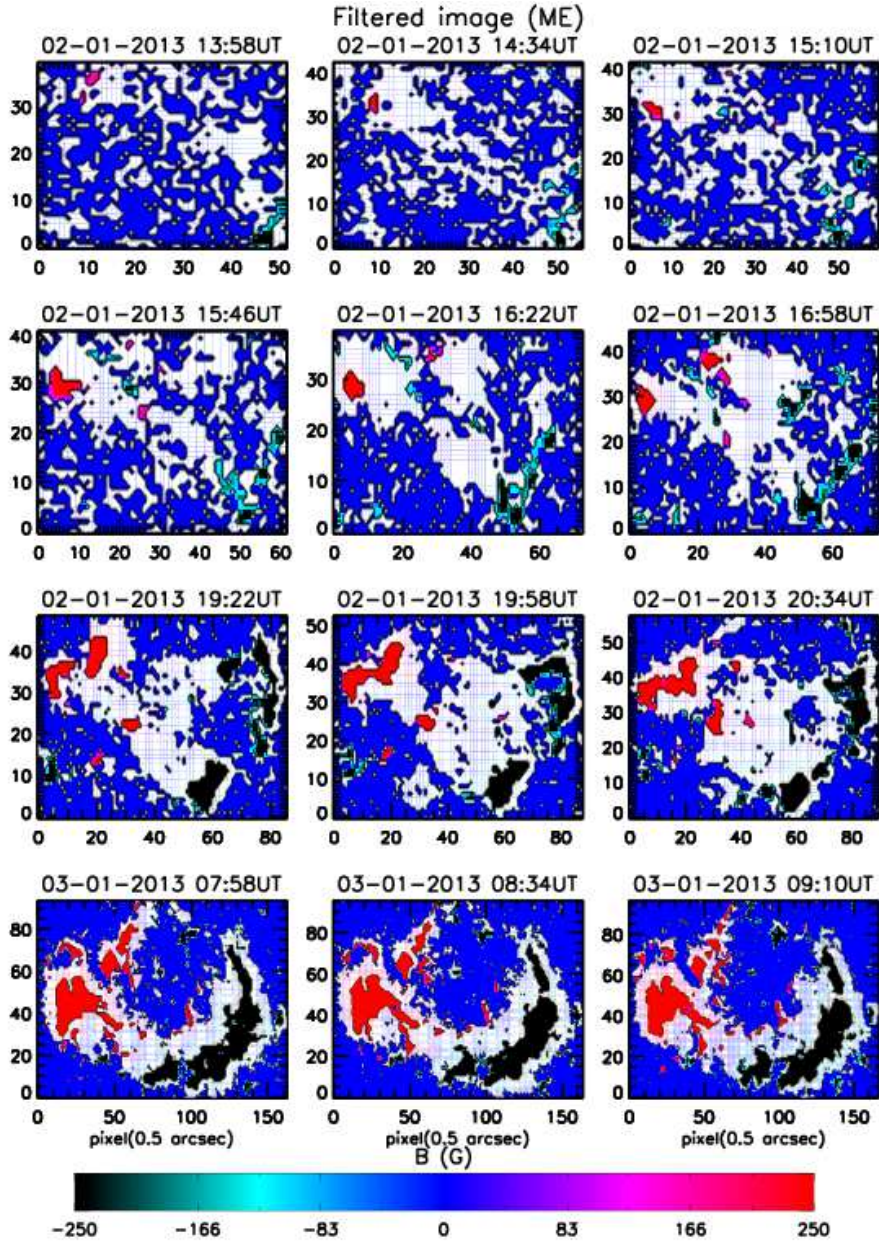


**Figure 9.** Results after filtering the weak-field regions. The total field lower than the threshold ( $|B| < |B|_{\text{thr}}$ ) is set to zero. These images correspond to the regions within the white boxes in Figure 7. The observation times are as indicated above the corresponding panels. The pixel size in both X and Y directions is 0.5 arcsec, as indicated in the X-axis labels in the last row. The areas with inclined field vectors ( $50^\circ < \theta_B < 130^\circ$ ) are painted in white to distinguish them from those with more vertically oriented field vectors. The quantity shown in the images is the line-of-sight component of the field, instead of the total field, to distinguish the two polarities.

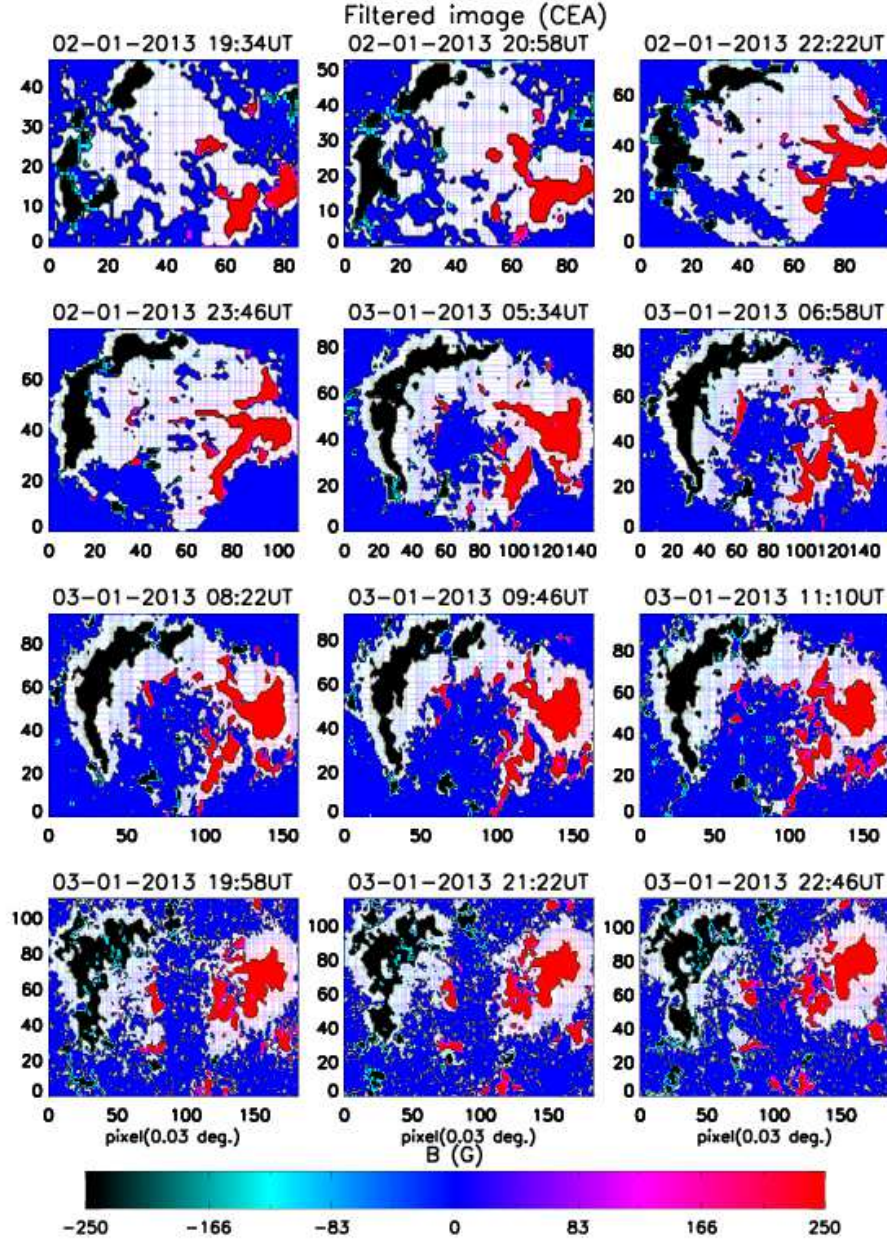


**Figure 10.** Results after filtering the weak-field regions. The total field lower than the threshold ( $|B| < |B|_{\text{thr}}$ ) is set to zero. These images correspond to the regions within the white boxes in Figure 8. The observation times are as indicated above the corresponding panels. The pixel size in both X and Y directions is 0.03 degree, as indicated in the X-axis labels in the last row. The areas with inclined field vectors ( $50^\circ < \theta_B < 130^\circ$ ) are painted in white to distinguish them from those with more vertically oriented field vectors. The quantity shown in the images is the radial component of the field, instead of the total field, to distinguish the two polarities.

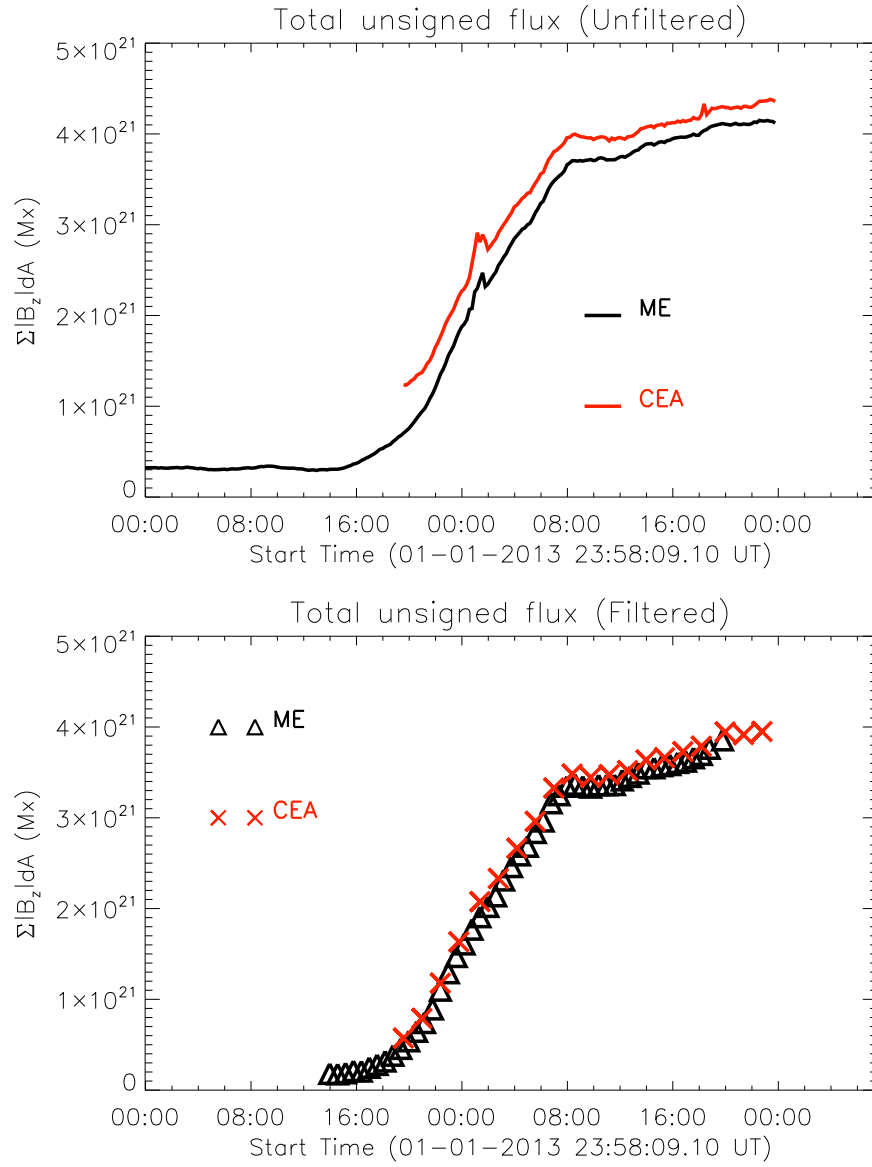


**Figure 11.** Temporal profile of the total unsigned flux of the analyzed region,  $F(t) = \sum |B_z| dA$ . The results computed from the ME and CEA magnetograms are shown in black and red, respectively. The upper panel shows the result of the original data without filtering, and the lower panel shows the result after the weak field,  $|B| < B_{\text{thr}}$ , has been filtered.

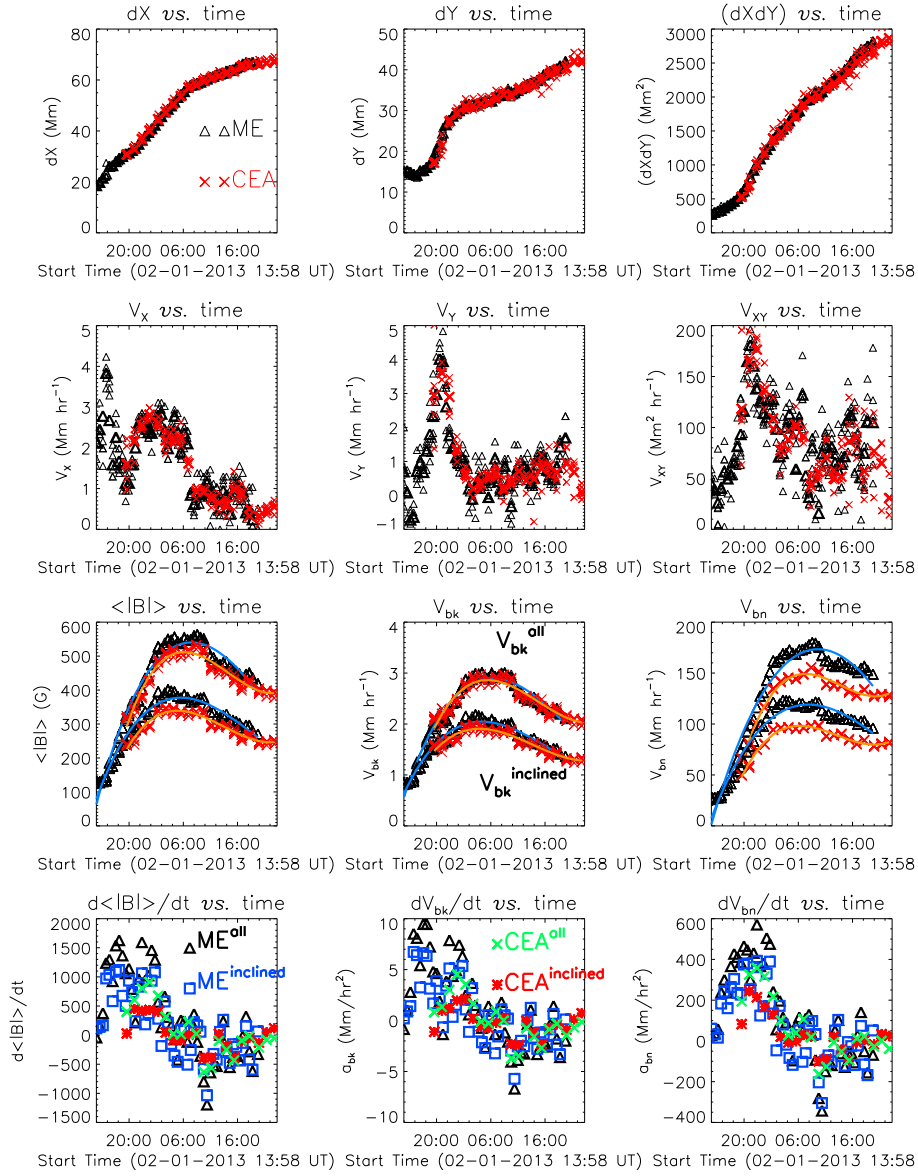


**Figure 12.** Measured quantities *vs.* time. The upper two rows show the quantities associated with the horizontal motions ( $dX$ ,  $dY$ ,  $(dXdY)$ , and their temporal derivatives), and the lower two rows show those associated with the vertical motions ( $\langle |B| \rangle$ ,  $V_{bk}$ ,  $V_{bn}$ , and their time derivatives).  $\langle |B| \rangle$ ,  $V_{bk}$ , and  $V_{bn}$  in the plots are the notations for the all-direction and inclined-field quantities. In the upper three rows, the red crosses and black triangles represent the results of CEA and ME data, respectively. In the upper two rows, the thinner symbols represent the results of individual edge-tracing of the X-t and Y-t plots to provide a visual measure of the uncertainties of the plotted quantities, and their averages are plotted as thicker ones to show their temporal profiles. In the third row, the higher curves correspond to the all-direction results, and the lower ones the inclined-field results. The solid lines are the results of a third degree polynomial fitting to the data. In the last row, black triangles, blue squares, green crosses and red stars represent  $ME^{all}$ ,  $ME^{inclined}$ ,  $CEA^{all}$  and  $CEA^{inclined}$ , as indicated

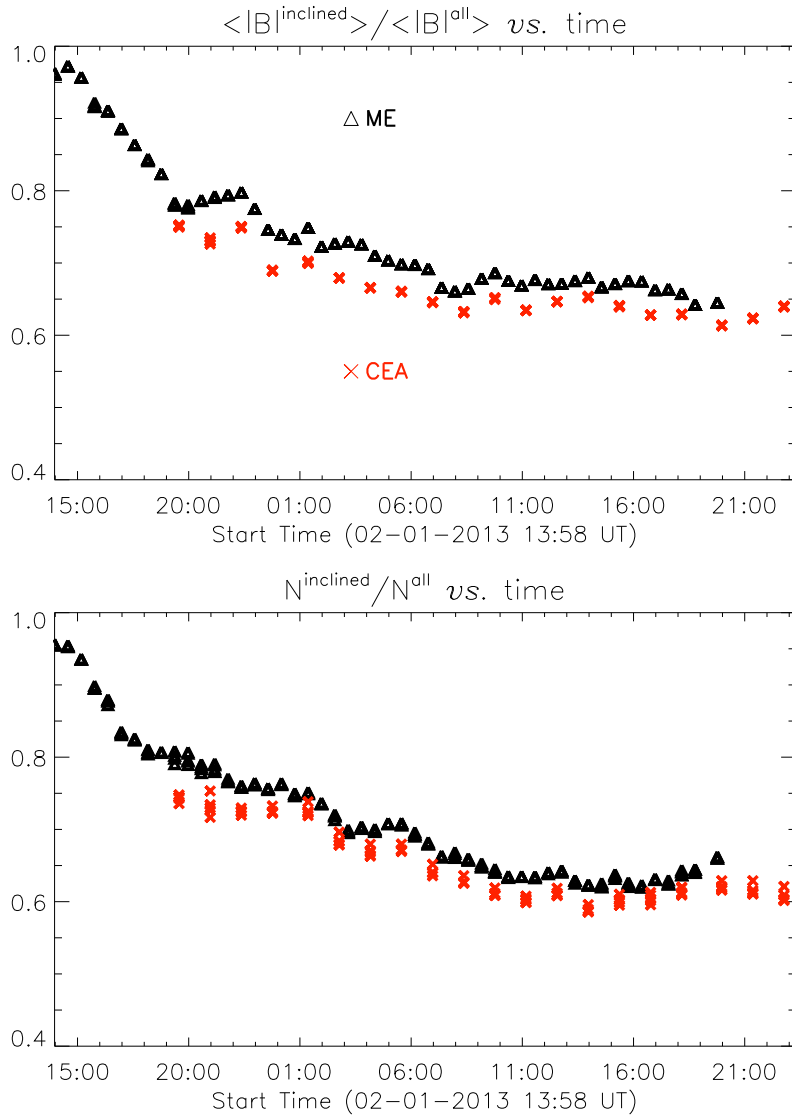


**Figure 13.** The temporal profiles of  $\langle |B|^{\text{inclined}} \rangle / \langle |B|^{\text{all}} \rangle$  (upper panel) and  $N^{\text{inclined}} / N^{\text{all}}$  (lower panel). The black triangles and red crosses represent the results of ME and CEA data, respectively. At each temporal point, there are five ME and five CEA data points, corresponding to the individual edge-tracing results of the X-t and Y-t plots. The level of the scattering of the data points provides a visual measure of the uncertainties of  $\langle |B|^{\text{inclined}} \rangle / \langle |B|^{\text{all}} \rangle$  and  $N^{\text{inclined}} / N^{\text{all}}$ .

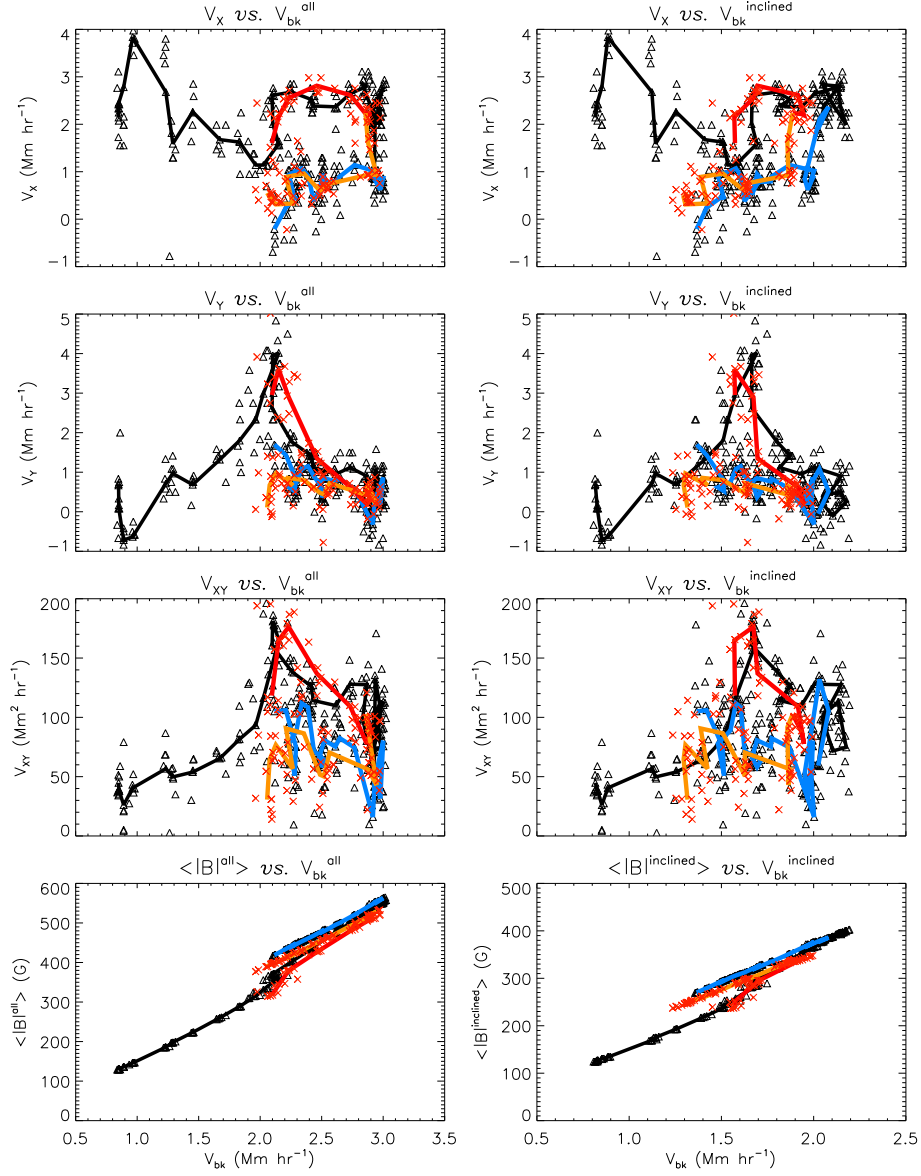


**Figure 14.** From top to bottom:  $V_X$ ,  $V_Y$ ,  $V_{XY}$  and  $\langle |B|^{all(inclined)} \rangle$  vs.  $V_{bk}^{all(inclined)}$ . The all-direction and inclined-field results are in the left and right columns, respectively. Red crosses and black triangles correspond, respectively, to the CEA and ME results of the individual edge tracings to provide a visual measure of the uncertainties of the plotted quantities. The averages of the individual tracings are joined by thick lines to show their profiles. The profiles before the peak of  $\langle |B|^{all} \rangle$  are plotted in black for the ME results and red for the CEA results. After the peak of  $\langle |B|^{all} \rangle$ , the ME and CEA profiles are plotted in blue and orange, respectively.

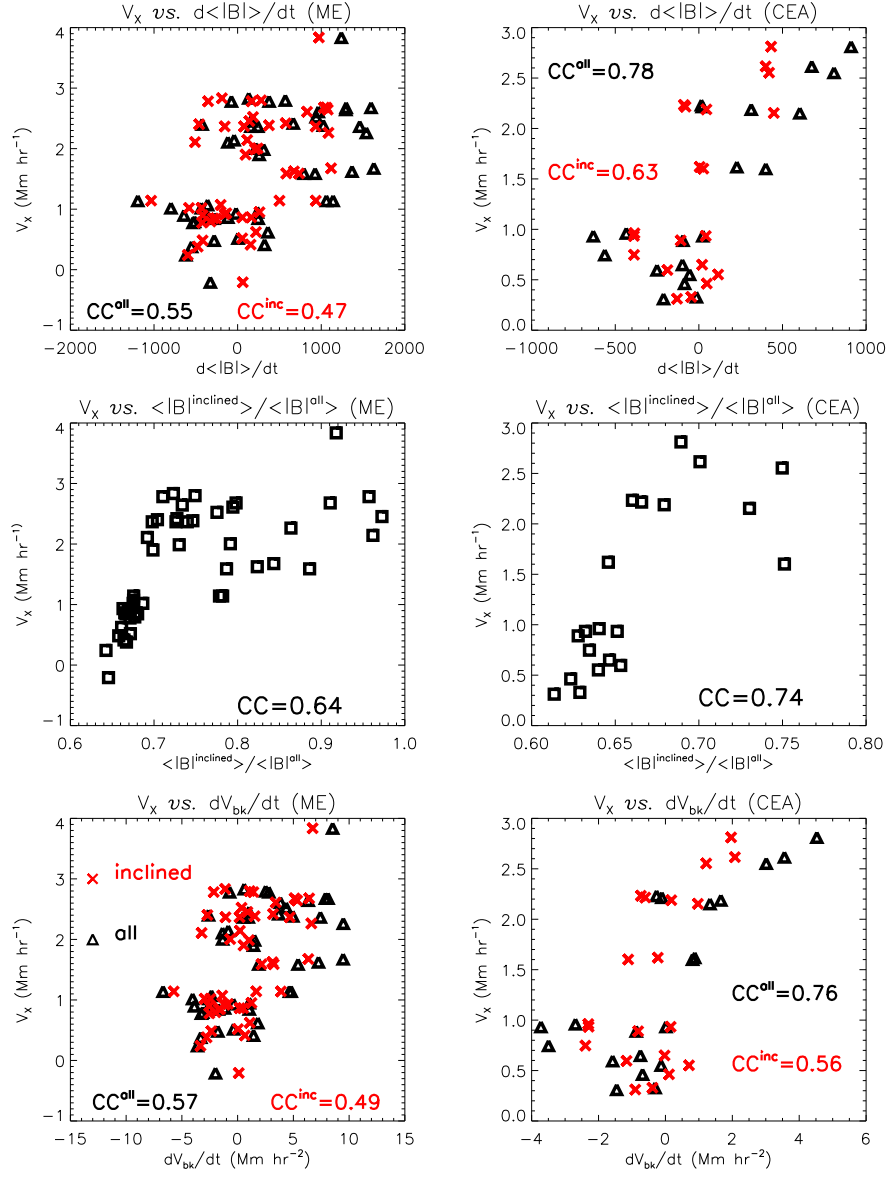


**Figure 15.**  $V_X$  vs.  $d\langle|B|\rangle/dt$  (top row),  $\langle|B|^{\text{inclined}}\rangle/\langle|B|^{\text{all}}\rangle$  (middle row), and  $dV_{\text{bk}}/dt$  (bottom row).  $d\langle|B|\rangle/dt$  is the notation for  $d\langle|B|^{\text{all}}\rangle/dt$  (black triangles) and  $d\langle|B|^{\text{inclined}}\rangle/dt$  (red crosses), and  $dV_{\text{bk}}/dt$  is the notation for  $dV_{\text{bk}}^{\text{all}}/dt$  (black triangles) and  $dV_{\text{bk}}^{\text{inclined}}/dt$  (red crosses). The results of ME and CEA data are in the left and right columns, respectively. The computed correlation coefficients (CC) are shown in respective panels.